Bulletin of the Seismological Society of America, Vol. 92, No. 4, pp. 1450–1469, May 2002

Interactions between the Landers and Hector Mine, California, Earthquakes from Space Geodesy, Boundary Element Modeling, and Time-Dependent Friction

by Evelyn J. Price and Roland Bürgmann

Abstract The M_w 7.1 Hector Mine earthquake happened 7 years after the 1992 M_w 7.3 Landers earthquake, within a system of right-lateral strike slip faults comprising the Eastern California Shear Zone. Because estimates of recurrence intervals of M 7 earthquakes on these faults range anywhere from 1500 to 50,000 years, the close temporal spacing of these two earthquakes suggests that there is some interaction between the two. Current models of simple Coulomb static stress interactions between the earthquake ruptures do not predict an obvious cause-and-effect relationship. The interaction between the computed normal and right-lateral shear stress reductions induced by the Landers earthquake at the Hector Mine hypocenter is unclear.

We use a combination of space geodesy, boundary element modeling, and computer modeling of time-dependent fault friction to investigate the interaction between the two earthquakes. We compare stress changes on the Hector Mine rupture plane induced by the Landers earthquake with the detailed slip distribution inferred using a combination of GPS and InSAR data. The slip distributions of both earthquakes are also used to infer the magnitude of the shear stress drop on each earthquake rupture and the orientation of the remote background stress consistent with these two recent events. For each earthquake the azimuth of the remote maximum compressive stress was approximately 17° ± 6°, and the magnitude of the shear stress drop was 8 ± 1 MPa on the Landers rupture and 10 ± 2 MPa on the Hector Mine rupture. Using a simple spring-and-slider model as a proxy for the rate-and-state frictional response of the Hector Mine faults to Landers earthquake-imposed stress steps, we find that, while a decrease in normal stress at the Hector Mine hypocenter would, by itself, have caused the Hector Mine earthquake to nucleate immediately, the simultaneous decrease in shear stress may have caused a delay in the peak shear loading. Consideration of an acceptable range of rate-and-state friction parameters, secular strain rates, and crustal stiffnesses leads us to conclude that this delay could have been 0 to 40 years.

Introduction

The 16 October 1999 M 7.1 Hector Mine earthquake broke more than 50 km of fault segments, including the newly named Lavic Lake fault and the Bullion fault in California's Mojave Desert (Scientists of the USGS *et al.*, 2000) (Fig. 1). This happened just 7 years after and 30 km to the east of the 1992 M 7.3 Landers earthquake rupture in a system of right-lateral strike-slip faults that are part of the Eastern California Shear Zone (ECSZ). The ECSZ is approximately 100 km wide and accommodates 14% to 21% of the shear between the North American and Pacific plates at the latitude of the Mojave Desert (Sauber *et al.*, 1986; Savage *et al.*, 1990; Sauber *et al.*, 1994; Hearn and Humphreys, 1998).

Paleoseismologic estimates of the recurrence intervals of clusters of earthquakes in the Mojave Desert near the Landers rupture are in the range of 5,000 to 15,000 years (Rockwell *et al.*, 2000). In contrast, it is possible that the Lavic Lake fault has not broken for the last 50,000 years (Thomas Rockwell, personal comm. 2000; Lindvall *et al.*, 2001). Geodetic measurements across the Mojave Desert indicate that the strain rate is spatially variable and is highest near the Landers earthquake rupture, with a value of 0.2

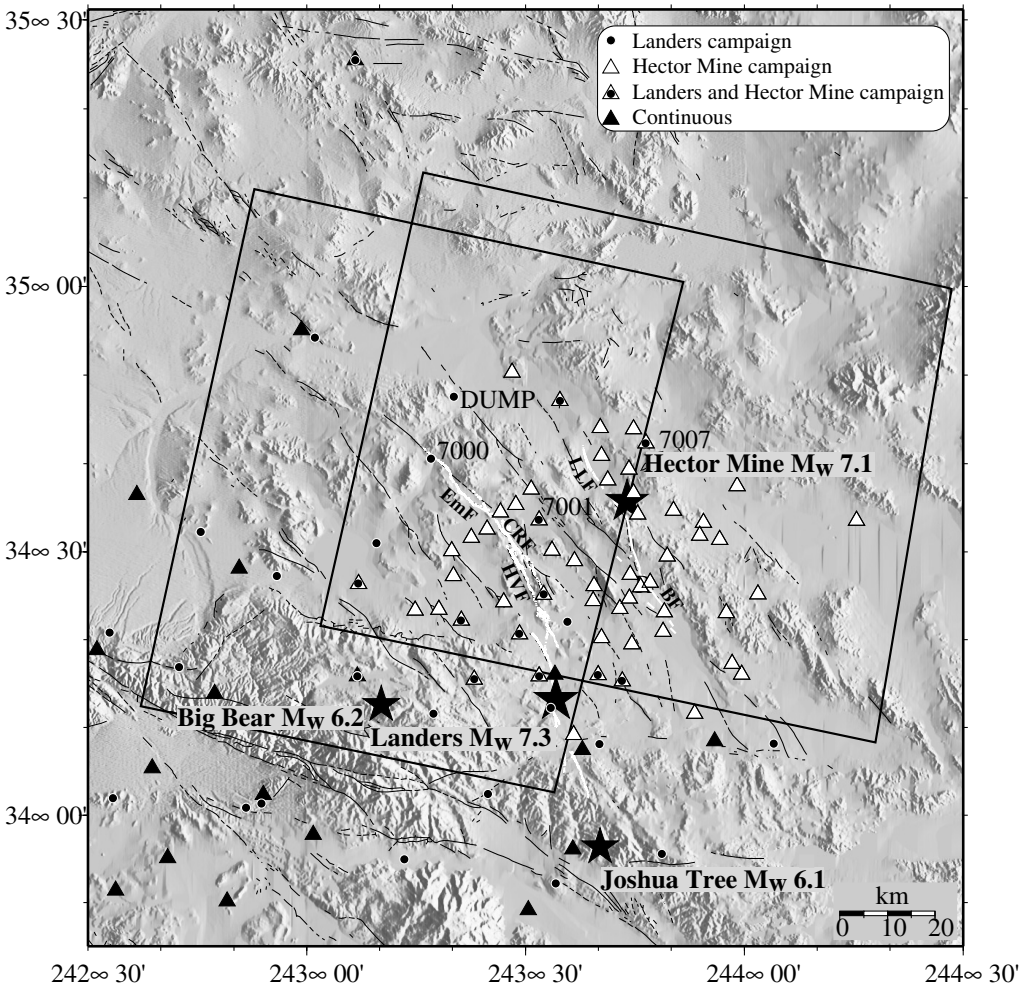

Figure 1. A shaded-relief map of the study area. The white lines indicate the traces of the Landers and Hector Mine surface ruptures. The black lines indicate faults mapped previously to the Landers earthquake. The black boxes outline the areas of the SAR data frames used to make interferograms. Triangle and dot symbols are at the locations of GPS sites as indicated in the legend. GPS sites discussed in the text (7000, 7001, 7007, and DUMP) are labeled. Stars mark the locations of regional earthquakes with magnitudes greater than 6 that have happened between 1992 and 2000. Abbreviations: Bullion fault (BF), Camp Rock fault (CRF), Emerson fault (EmF), Homestead Valley fault (HVF), Lavic Lake fault (LLF).

μrad/yr, and lower near the Hector Mine rupture, with a value of 0.06 μrad/yr (Sauber *et al.*, 1986, 1994; Savage *et al.*, 1990). Modeling of these strain observations implies that there is a zone of distributed shear beneath the Mojave Desert and that the faults that broke during the Hector Mine earthquake lie near the eastern edge of this zone (Sauber *et al.*, 1994).

Spatial and temporal changes in the rate of seismicity following the Landers earthquake indicate that its occurrence changed the state of stress in the Mojave Desert (Hauksson, 1994; Wiemer and Wyss, 1994; Gross and Kisslinger, 1997; Wyss and Wiemer, 2000). With regards to the Hector Mine rupture, calculations of the static Coulomb stress changes induced along it by the Landers earthquake indicate that, in general, the Landers earthquake made it less likely that the faults involved in the Hector Mine rupture would break (Scientists of the USGS *et al.*, 2000; Parsons and Dreger, 2000; Harris and Simpson, 2002). In spite of this, there was a cluster of Landers aftershocks near the future Hector Mine hypocenter (Hauksson *et al.*, 1993), indicating a local increase in tendency for failure. This observation is not in accord with current conceptual models of static stress triggering, which predict a decrease in seismicity in the stress shadow (region of stress decrease) of a large earthquake (e.g., Harris and Simpson, 1998).

Given the millennial-scale earthquake recurrence intervals, the fact that the Hector Mine rupture happened only 7 years after the Landers rupture, the 30-km distance between the two earthquake ruptures, and the changes in rate of microseismicity, it is likely that there is a mechanical link between the Hector Mine and Landers earthquakes. Considering what we know about the mechanics of the Earth's

faulted crust, this link can be investigated using a combination of models that consider the effects of stress transfer through the lithosphere, frictional properties of the faults along the Hector Mine rupture, and lower crustal and upper mantle structure. Other workers have considered the loading effects of postseismic viscoelastic deformation of the lower crust and upper mantle after the Landers earthquake on the faults that broke during the Hector Mine earthquake (Freed and Lin, 2001; Wang and Jackson, 2000; Pollitz and Sacks, 2002). Here we consider the effects of the static stress induced by the Landers earthquake on the Hector Mine rupture (e.g., Parsons and Dreger, 2000; Scientists of the USGS *et al.*, 2000; Harris and Simpson, 2002), and the rate-and-state dependent frictional response of the Hector Mine faults.

The recent advent and development of space geodetic techniques that map displacement fields of the Earth's surface with unprecedented spatial and temporal accuracy and high precision makes it possible for us to explore the mechanics of faulting in detail. Here, we use a combination of measurements made using the Global Positioning System (GPS) and synthetic aperture radar interferometry (InSAR) to infer detailed distributions of lateral slip on the Hector Mine and Landers earthquake ruptures. We use the slip estimates as the boundary conditions in linear, homogeneous elastic half-space boundary element models to predict the change in loading caused by Landers on the Hector Mine earthquake rupture and to infer the ambient background stress. We then use these stress fields along with the geodetically and geologically inferred strain rates as initial conditions in rate-and-state dependent fault friction models to describe the time-dependent effects of the Landers-induced stress field on the Hector Mine earthquake faults. We find that time-dependent frictional loading of the Hector Mine hypocenter resulting from the changes in static stress caused by Landers could have made it more likely that the Hector Mine earthquake would nucleate where and when it did.

The Geodetic Data

The deformation of the Earth's surface in the region surrounding the Hector Mine and Landers ruptures was measured using GPS and InSAR techniques. In general, the temporal and spatial sampling and errors in the geodetic measurements vary. Although the largest signal in the geodetic displacement measurements is caused by coseismic deformation, significant displacements can be generated by interseismic and postseismic deformation.

GPS displacements provide unambiguous three-dimensional displacement vectors, but are sparsely sampled in space. Campaign GPS sites are more spatially dense than continuous GPS stations, but the measurements can span years before to months after an earthquake. In contrast, continuous GPS displacement measurements provide high temporal sampling, so they record all of the phases of the earthquake cycle. The errors in the GPS measurements are relatively well known. Precisions of 2 mm in horizontal components and 1 cm in vertical components of displacement are routinely attained using continuous GPS. The precisions of displacement measurements made using campaign GPS vary depending on factors such as site occupation times, conscientiousness of the human operator, number of satellites in view, type of GPS antenna–receiver package, and stability of monuments. The precisions of the displacements measured at most sites using dual-frequency GPS receivers are 10 mm or better for both the Landers and Hector Mine data sets.

Interferometric synthetic aperture radar is a quickly emerging geodetic technology. Using InSAR processing methods, we combine two satellite radar images taken before and after an earthquake to estimate the displacement of the Earth's surface at 30-m postings over a 100-km-wide area with centimeter precision in the direction of the radar's line of sight (LOS). An interferogram records differences in the range (the apparent distance from the satellite to the ground and back) at the two times of imaging.

The vector connecting the positions of the satellite during the first and second passes is called the interferometric baseline. If the baseline is greater than zero, the measured changes in range are due to topography, deformation, and noise. To measure deformation, the topographic contribution to the change in range must be computed using ancillary elevation data and then removed from the interferogram. The noise in interferometric measurements caused by decorrelation of the radar signals received at the two times of imaging and the errors in elevation used to compute the topographic contribution to the range change increase as the component of the baseline perpendicular to the radar's LOS increases. Thus, for deformation mapping, it is desirable that the perpendicular baseline component be small. InSAR LOS displacement estimates have been compared to their counterparts made using GPS techniques, and it has been found that they agree at the 1-cm level (e.g., Zebker *et al.*, 1994).

The displacement vectors measured using the InSAR technique are well sampled in space, but the displacement is measured only in the direction of the radar's LOS. Horizontal deformations can be interpreted as vertical deformations and vice versa. The measurements are from three times to infinitely more sensitive (e.g., horizontal displacements parallel to the radar's flight path cannot be detected) to vertical deformations than they are to horizontal deformations, depending on the orientation of the horizontal displacement (e.g., Price, 1999a). While there is a possibility that an interferogram could be formed every 35 days using images from every pass of the first and second European Remote Sensing satellites (ERS-1 and ERS-2), sometimes the separation between the positions of the satellite during the two imaging passes is so large that the images do not correlate (for ERS imagery, the theoretical maximum baseline length is 1 km). Because we generally do not have readily available multiple observations over time windows spanning events, it is difficult to assess all the errors in our measurements, but they are generally at the 1-cm level (as noted earlier in this section).

GPS Measurements

Landers Earthquake

We use the internally consistent GPS displacement solution of Freymueller *et al.* (1994) in the inversion for distributed slip on the Landers earthquake rupture. They computed 38 displacements relative to the continuous GPS site at Vandenburg Air Force Base (located approximately 375 km from the epicenter). The GPS sites consist of 7 within the California Department of Transportation High Precision Geodetic Network (HPGN), 15 within the San Bernardino County Surveyor's Office GIMMS network (SBCO), 5 that are part of the Caltech and County Surveyors' Inter-County surveys (CIT), 6 installed by the United States Geological Survey (USGS), and 5 that are continuously operating as part of the Permanent GPS Geodetic Array (PGGA). Details of the data sources are tabulated in Hudnut *et al.* (1994); details of the GPS processing are described by Freymueller *et al.* (1994).

Except for the SBCO sites, all of the sites were occupied before and after the earthquake with dual-frequency GPS receivers. The SBCO sites were occupied with single-frequency GPS receivers before the earthquake and dual-frequency GPS receivers after the earthquake. Unlike the measurements made using dual-frequency GPS receivers, it is difficult to mitigate the errors resulting from ionospheric noise in the positions of sites measured using single-frequency GPS. Thus, we discard displacements computed at SBCO sites 7000, 7001, and DUMP, whose pre-earthquake positions were measured on ionospherically noisy days (see Freymueller *et al.*, 1994), and include only 35 displacements in our inversion. Of these, 28 are shown in Figure 2; the rest are outside the geographic bounds of the map.

One source of error in coseismic GPS displacement measurements arises from the secular and postseismic strain that occurs before and after an earthquake during the time between occupations of the GPS sites. No contribution of secular strain was removed from the GPS displacements, although up to 3 cm of relative displacement from deformation associated with the San Andreas fault could have accumulated across the HPGN during the year between the pre-earthquake surveys and the earthquake. Half as much displacement could have accumulated across the SBCO GIMMS network, but this is less than the 3 to 5 cm uncertainty in the displacements computed using single-frequency data (Freymueller *et al.*, 1994). While postseismic deformation can occur on multiple temporal and spatial scales, depending on the deformation source (Shen *et al.*, 1994; Peltzer *et al.*, 1996; Savage and Svarc, 1997; Wdowinski *et al.*, 1997;), a large postseismic transient with an amplitude that was 10% of the coseismic displacement amplitude and a decay time of approximately 40 days was measured at continuous and campaign GPS sites (Shen *et al.*, 1994; Bock *et al.*, 1997; Savage and Svarc, 1997). Based on the postseismic occupation history of campaign GPS sites tabulated by Shen *et al.* (1994) and the 40-day decay-time model, up to 7 mm of postseismic displacement could have contaminated the coseismic measurements at locations near the rupture. We did not attempt to correct the GPS displacements for interseismic and postseismic strain, since the magnitudes of those contributions are less than the significant errors in the observations.

Hector Mine Earthquake

We use geodetic measurements made at 54 geodetic markers within a 50-km radius of the Hector Mine rupture that operate as campaign GPS (D. Agnew, personal comm., 2000) (Fig. 3) and at 144 stations maintained by the Southern California Integrated GPS Network (SCIGN) (some are shown in Fig. 3). Observed coseismic GPS displacements were as large as 90 cm and formed a pattern consistent with a right-lateral strike-slip event. The campaign-mode GPS markers were surveyed up to 2 years before the earthquake and within the 3 months following it; the SCIGN receivers are continuously operating. An interseismic correction was made to the campaign GPS displacements (Agnew *et al.*, 2002). While a coseismic displacement at site 7007 (Fig. 1) was available, we did not include it because the site was last surveyed, prior to the Hector Mine earthquake, 2 weeks after the Landers earthquake and so we expect that its displacement may be significantly contaminated by Landers postseismic deformation.

InSAR Measurements

Landers Earthquake

The interferogram spanning the Landers earthquake (Fig. 2) is composed of the classic pair of radar images recorded by the ERS-1 satellite and presented in early works on earthquake deformation mapping using InSAR (Massonnet *et al.*, 1993; Peltzer *et al.*, 1994; Zebker *et al.*, 1994; Price and Sandwell, 1998). The images in this pair were acquired on 24 April 1992 and 7 August 1992, spanning 65 days before to 40 days after the earthquake (Table 1). The component of the interferometric baseline perpendicular to the radar LOS is 130 m.

Hector Mine Earthquake

The interferogram spanning the Hector Mine earthquake (Fig. 3) is made from ERS-2 images spanning 31 days before to 4 days after the earthquake (Table 1). The component of the interferometric baseline perpendicular to the radar LOS is 23 m. The interferogram shown here is very similar to ones computed earlier by groups at the Jet Propulsion Laboratory (JPL), the California Institute of Technology (Caltech), Stanford University, and the University of California, San Diego (UCSD) (Peltzer *et al.*, 1999; Sandwell *et al.*, 1999; Simons *et al.*, 1999; Zebker *et al.*, 1999).

Joint Inversion of GPS and InSAR Data

We combine geodetic data sets in a damped linear least-squares inversion to infer the distributions of slip on the

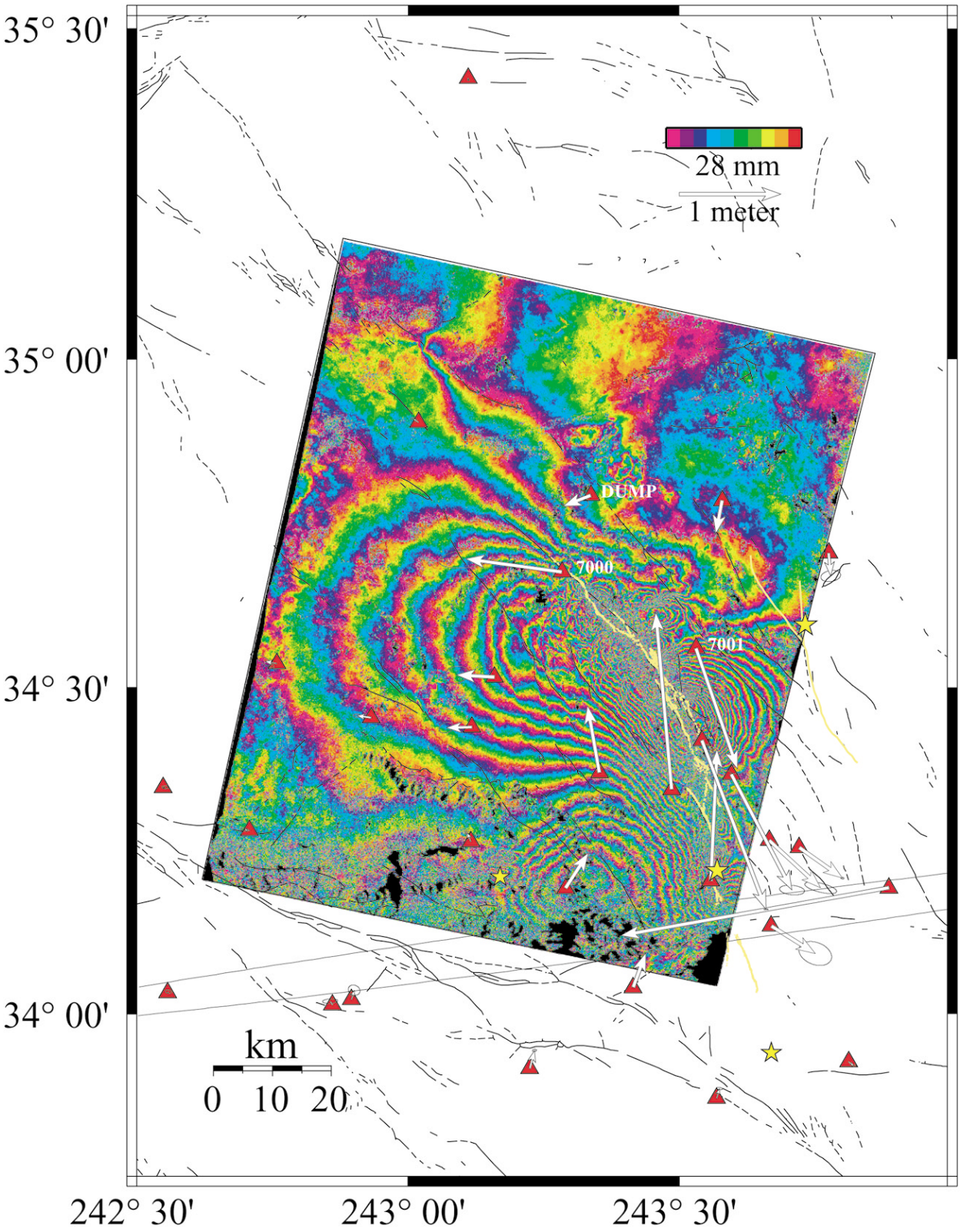

Figure 2. The InSAR and GPS data spanning the Landers earthquake. Stars mark the locations of the Joshua Tree, Landers, Big Bear, and Hector Mine epicenters. The red triangles are at the positions of GPS sites. The GPS displacements are from Freymueller *et al.* (1994). The SAR frame covering the Landers earthquake is outlined by a black rectangle. The yellow lines are the traces of the Landers and Hector Mine surface ruptures.

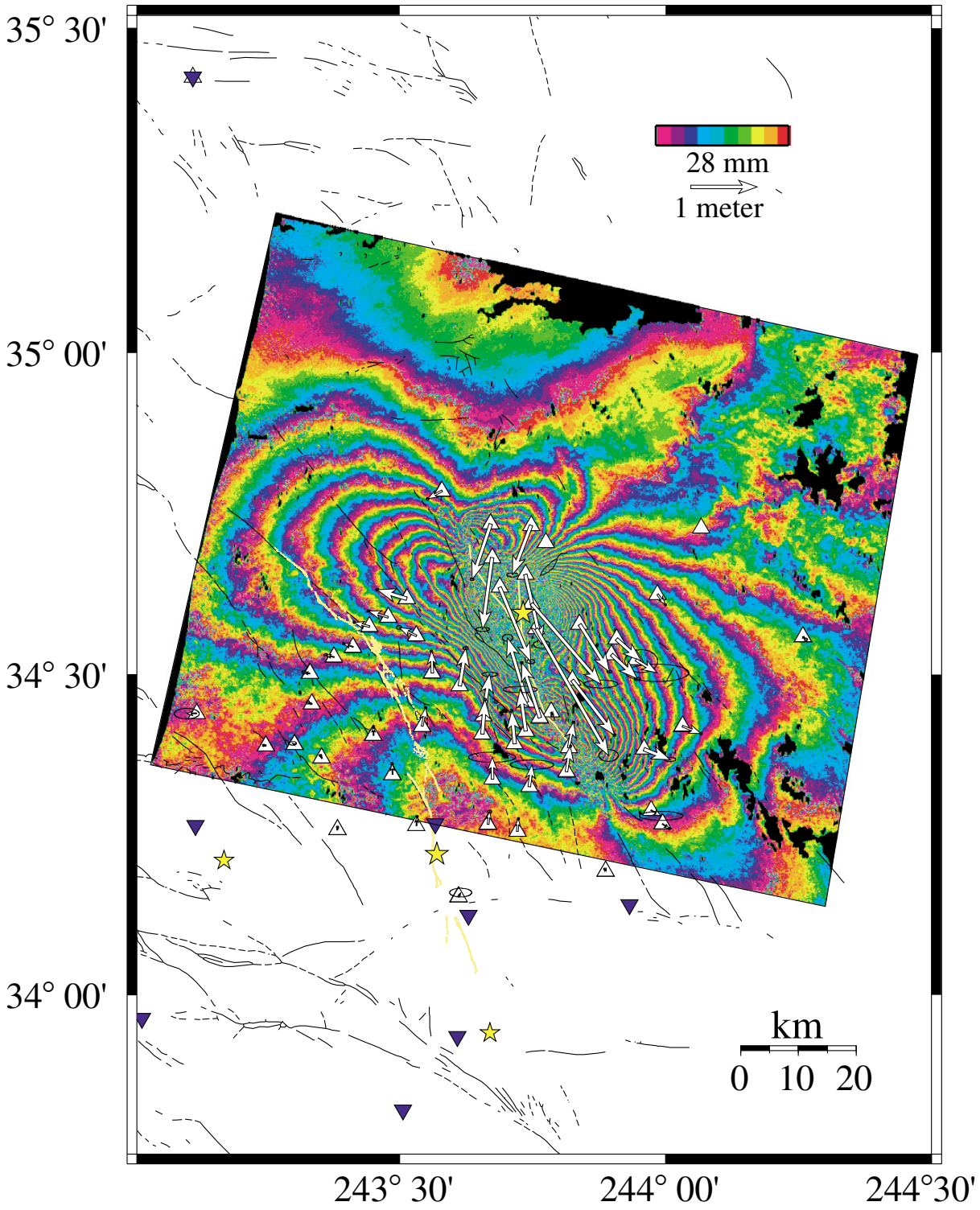

Figure 3. The InSAR and GPS data spanning the Hector Mine earthquake. The stars mark the locations of the Joshua Tree, Landers, Big Bear, and Hector Mine epicenters. The white triangles are at the positions of campaign GPS sites whose displacements were made available by Duncan Agnew (personal comm.). The blue triangles are at the positions of continuous GPS sites whose displacements were made available by SCIGN. The yellow lines show the traces of the Landers and Hector Mine surface ruptures.

Table 1
The Data Frames and Baseline Parameters Used in This Study

Reference		Repeat		Perpendicular Baseline
Satellite: Orbit_Frame	Acquisition Date	Satellite: Orbit_Frame	Acquisition Date	Length (m)
ERS1: 5554_2907	7 Aug. 1992	ERS1: 4051_2907	24 Apr. 1992	130
ERS2: 23027_2907	15 Sep. 1999	ERS2: 23528_2907	20 Oct. 1999	23

Hector Mine and Landers earthquake ruptures. We include geologically measured coseismic fault offsets; constrain the slip to be right-lateral and to be in the 0 to 8 m range using a bounded variables least squares algorithm (Stark and Parker, 1995). A homogeneous, linear elastic half-space Earth model containing a vertical cut describes the assumed physics of the problem for each earthquake. Each cut is a synthetic earthquake rupture plane whose trace, at the surface of the half-space, follows the geometry of the rupture mapped at the Earth's surface by geologists. For each rupture, the cut extends to 20-km depth; we do not include overlapping segments. We assume that each rupture is a continuous surface. We divide each rupture surface into abutting 2- by 2-km patches (shown in Figs. 4 and 5). Using planar, rectangular patches to parameterize the rupture enables us to use the formulation of Okada (1985) to predict the displacements at the surface of the half-space caused by offsets across each patch. Since a displacement measured at the surface is a linear sum of the surface displacements predicted by the offsets across each patch, we can use linear inversion techniques to infer the distribution of slip on an earthquake rupture. In all of our elastic Earth models, the Poisson's ratio is 0.25 and the shear modulus is 30 GPa.

To infer the distribution of slip on the earthquake ruptures we solve the following system of equations for the elements of $\vec{\mathbf{m}}$, c, s_e, and s_n:

$$\begin{bmatrix} C_g\Sigma_{gps}^{-1/2} & [\mathbf{G}_{gps} & \mathbf{0}] \\ C_s\Sigma_{sar}^{-1/2} & [\mathbf{G}_{sar} & \mathbf{P}] \\ \beta_j & [\mathbf{L} & \mathbf{0}] \end{bmatrix} \begin{bmatrix} \vec{\mathbf{m}} \\ c \\ s_e \\ s_n \end{bmatrix} = \begin{bmatrix} C_g\Sigma_{gps}^{-1/2}\vec{\mathbf{d}}_{gps} \\ C_s\Sigma_{sar}^{-1/2}\vec{\mathbf{d}}_{sar} \\ \mathbf{0} \end{bmatrix}, \quad (1)$$

where C_g is the relative weight of GPS data; C_s is the relative weight of InSAR data; $\mathbf{\Sigma}_{gps}$ is the GPS data covariance matrix; $\mathbf{\Sigma}_{sar}$ is the InSAR data covariance matrix; $\mathbf{G}_{gps}$ is the GPS design matrix; $\mathbf{G}_{sar}$ is the InSAR design matrix; $\mathbf{P}$ allows for a regional tilt in the InSAR displacement map; β_j controls the smoothness of the model; $\mathbf{L}$ is a discretized Laplacian filter; $\vec{\mathbf{m}}$ contains the coefficients of the distributed slip model; c, s_e, and s_n are, respectively, a constant offset, east slope, and north slope in the InSAR displacement map; $\vec{\mathbf{d}}_{gps}$ contains the GPS displacements; and $\vec{\mathbf{d}}_{sar}$ contains the InSAR displacements, which are subsampled from the original displacement maps at 1-km spacing. The design matrices contain the Green's functions, which relate displacements at geodetic measurement locations to slip on rupture patches.

The GPS covariance matrices contain the variance of the displacement measurements and the covariances between east and north displacement components at each GPS site. The InSAR covariance matrices are constructed by assuming that the variance of each measurement is 1 cm^2 and that there is no covariance between measurements. While there may be correlations between the errors in the InSAR measurements due to atmospheric noise, it is difficult to characterize these errors, since the spatial resolution of techniques (e.g., GPS–meteorology) used to estimate spatial variations in both the ionosphere and troposphere does not approach the resolution of the data (Williams *et al.*, 1998; Hanssen, 1998; Emardson *et al.*, 1999). We mitigate any covariance-related bias in our InSAR inversions by significantly subsampling the interferogram (e.g., Lee *et al.*, 1992). Atmospheric errors can be 5 cm in size (e.g., Tarayre and Massonnet, 1996).

Model Smoothing and Data Combination

When we estimate the distribution of slip on the earthquake rupture surfaces we encounter the technical issues of model smoothing and data combination. We first infer the slip distribution using GPS and InSAR measurements individually and analyze groups of distributed slip models in which the smoothness of the members differ. As the roughness of the model decreases, the misfit between the surface displacements predicted by the model increases and our variance reduction is less (Fig. 6). We choose, from each individual group of models, an optimal member that retains enough detail, is reasonably smooth, and maintains an acceptable level of misfit. This approach is common and is similar to the one suggested by Harris and Segall (1987) and Du *et al.* (1992), who choose a value of the smoothing near the location on the tradeoff curve where little decrease in misfit (or variance reduction) is gained by adding more roughness to the model. Optimal members of the InSAR and GPS groups are shown in the top two panels of Figures 4 and 5, and their values of roughness and misfit are indicated by arrows on Figure 6. After we have chosen the optimal group members, we weight the data sets in a joint inversion such that the amount of roughness specified by the optimal members of the individual data-type inversions is maintained.

To elucidate, when we perform an individual data-type inversion, we minimize

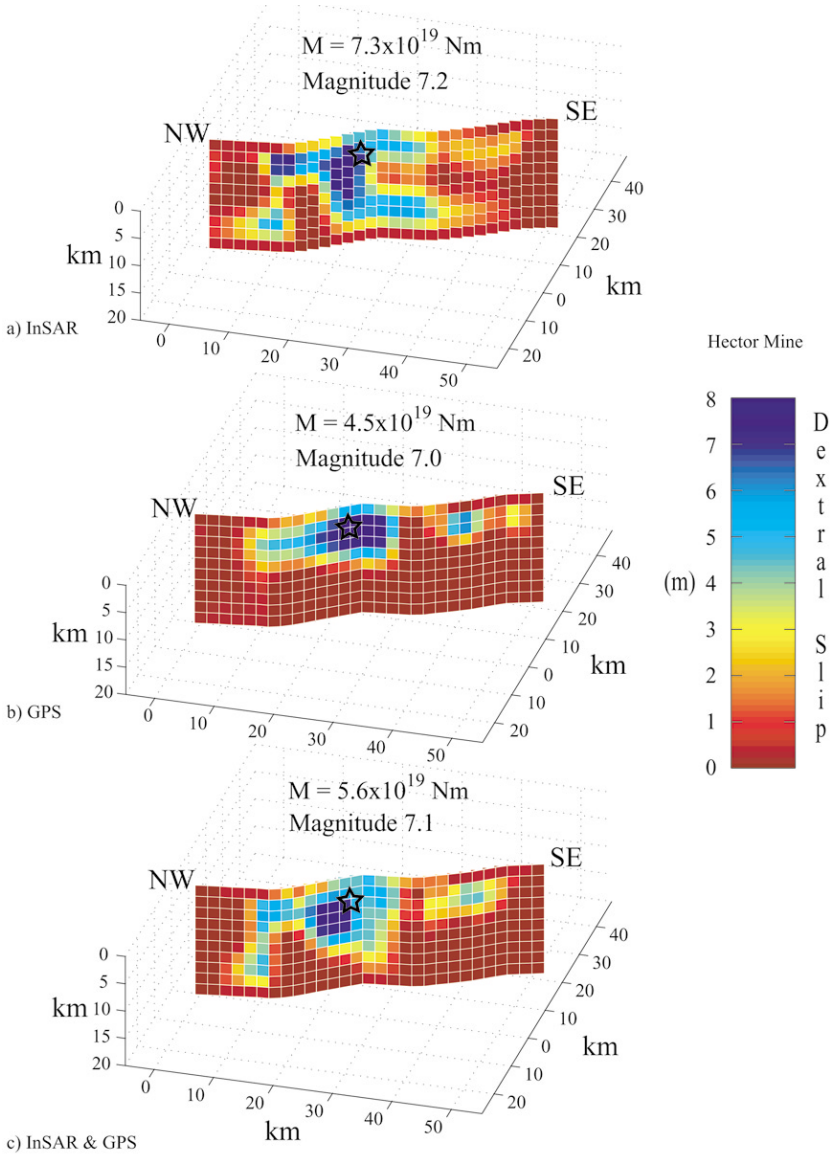

Figure 4. The preferred distributions of slip on the Hector Mine rupture inferred from (a) InSAR displacements, (b) GPS displacements, and (c) joint inversion of InSAR and GPS displacements.

$$\|\sum^{-1/2}(\mathbf{G}\vec{\mathbf{m}} - \vec{\mathbf{d}})\| + \beta_j^2\|\mathbf{L}\vec{\mathbf{m}}\|, \qquad (2)$$

where $\vec{\mathbf{d}}$ holds either GPS or InSAR data. The terms inside the double bars are called the misfit and the roughness (on the left and right, respectively). When we perform the joint inversion, we use two data types but require only one smoothing factor and determine data weights, C_g and C_s, that force the contribution of each data type to the roughness-to-misfit ratio of the joint model to be the same as in the single-data-type inversions. As a result, equal weight is given to each individual data set according to the weighting parameters of each individual optimally smoothed distributed slip model. For example, we first choose $\beta_j = 0.8$. If, for our chosen models in the individual data-type inversions, $\beta_{gps}/C_g = 0.4$ and $\beta_{sar}/C_s = 0.04$, then, in the joint inversion $\beta_j = \beta_{gps} + \beta_{sar}$ and $\beta_{gps} = \beta_{sar}$, so that $C_g = 1$ and $C_s = 10$. Using this weighting scheme, we infer the slip distributions shown in the lower panels of Figures 4 and 5. This weighting scheme is the same as that described by Kaverina *et al.* (2002).

Model Resolution

The determination of the model resolution on the synthetic rupture surface is a tool for interpreting distributed slip models, which helps us to understand the spatial wavelength of inferred variations of slip that are likely to be real. Resolution varies spatially along the rupture surface and with depth (e.g., Du *et al.*, 1992; Harris and Segall, 1987). If we assume that the rupture plane geometry is correct and that the Earth is a homogeneous, linear elastic half-space, the model resolution depends on the spatial distribution of displacement measurements at the Earth's surface, the errors in those measurements, and our chosen value for model smoothing (β). The resolution of slip distributions inferred using sparsely distributed, pointwise geodetic measurements is generally low at depths greater than 5–10 km. Because

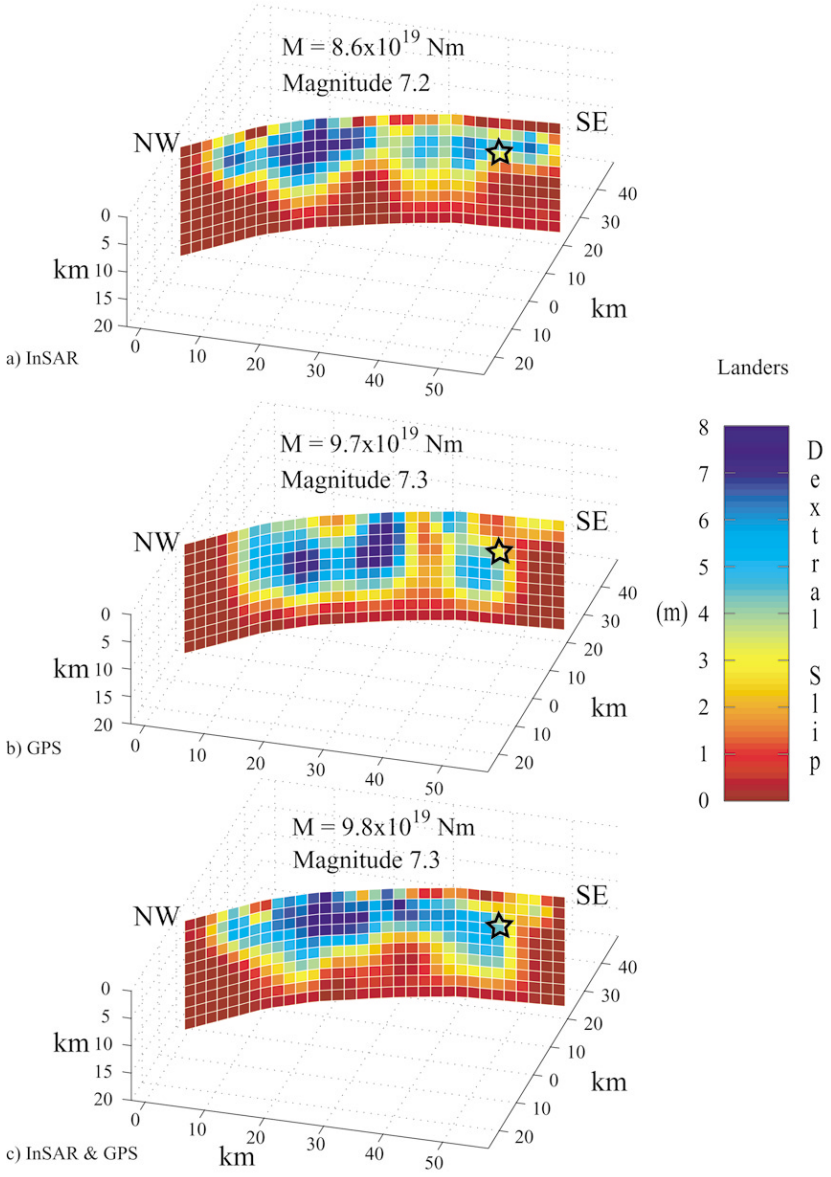

Figure 5. The preferred distributions of slip on the Landers rupture inferred from (a) InSAR displacements, (b) GPS displacements, and (c) joint inversion of InSAR and GPS displacements.

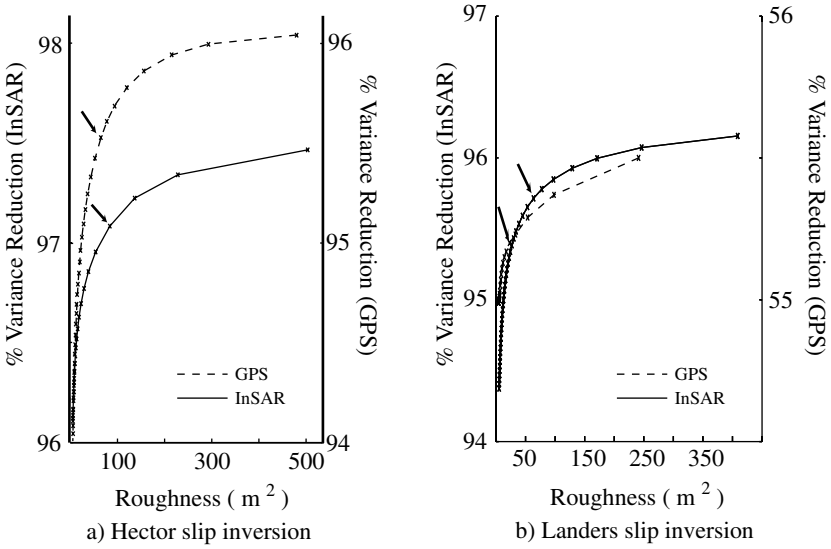

Figure 6. The dependence of the reduction in data variance on model roughness. In each graph, the arrows point to the locations on the curves corresponding to the values of roughness and variance reduction of our favored models. (a) The graph corresponding to the Hector Mine data inversion. (b) The graph corresponding to the Landers data inversion.

the spatial distribution of InSAR measurements is dense, we expect to achieve higher resolution in our inversions than in those that use GPS data alone. Because our knowledge of the InSAR covariance matrix is poor, we consider only the effect of the distribution of displacement measurements and an assumed rupture geometry on our model resolution.

In an ideal world with noiseless data and perfect Green's functions of a linear elastic Earth, each datum would be a linear sum of the offsets across each model patch: $\mathbf{G}_i\vec{\mathbf{m}}_i = \vec{\mathbf{d}}_i$. In actuality, the Earth is heterogeneous, layered, and sometimes anelastic; our rupture geometry is not perfect; and a straight linear inversion would assume that we can resolve variations in slip with spatial wavelengths of 4 km. Since we approximate the Earth as a linear elastic half-space, we infer the distribution of slip by applying an inversion filter to our data, which is smoothed by a Laplacian filter (Equations 1 and 2) whose weight is determined based on trade-offs between data misfit and model roughness (e.g., Fig. 6). The distributed slip model perceived through our smoothed inversion filter is $\vec{\mathbf{m}}_p = \mathbf{G}_p^{-1}\vec{\mathbf{d}}_p$.

If we assume that the InSAR and GPS displacement measurements are perfect (the resolution depends only on the spatial distribution of measurements), then the effect of our smoothed inversion filter on the ideal distribution of slip is $\vec{\mathbf{m}}_p = \mathbf{G}_p^{-1}\mathbf{G}_i\vec{\mathbf{m}}_i$. Given the geometry of the rupture and our smoothing weight, our resolution matrix, $\mathbf{R} = \mathbf{G}_p^{-1}\mathbf{G}_i$, converts a synthetic distributed slip model to the model we would infer given the locations of our observations and our smoothing weight (Fig. 7).

Landers and Hector Mine Slip distributions

Landers. Our distributed slip model for the Landers earthquake derived from the joint inversion of GPS and InSAR data is shown in Figure 5. The overall pattern of slip is similar to that obtained using other geophysical methods (e.g., Cohee and Beroza, 1994; Wald and Heaton, 1994), in that most of the slip is inferred north of the hypocenter near the step-over between the Homestead Valley and the Camp Rock faults. While it is likely that the rake of fault slip was not exactly 180°, especially near the ends of the rupture and in fault step-overs, vertical slip is not well resolved using current geophysical methods. Vertical displacements across the rupture were measured at several locations in the field (Hart *et al.*, 1993; Irvine and Hill, 1993; Sieh *et al.*, 1993; Arrowsmith and Rhodes, 1994; Johnson *et al.*, 1994; Aydin and Du, 1995; Sowers *et al.*, 1994; Spotila and Sieh, 1995; Zachariasen and Sieh, 1995; Fleming and Johnson, 1997; McGill and Rubin, 1999), but they are typically near restraining or tensional bends in the rupture and are likely to be local features only.

Using the InSAR data alone, the inferred slip (Fig. 5a)

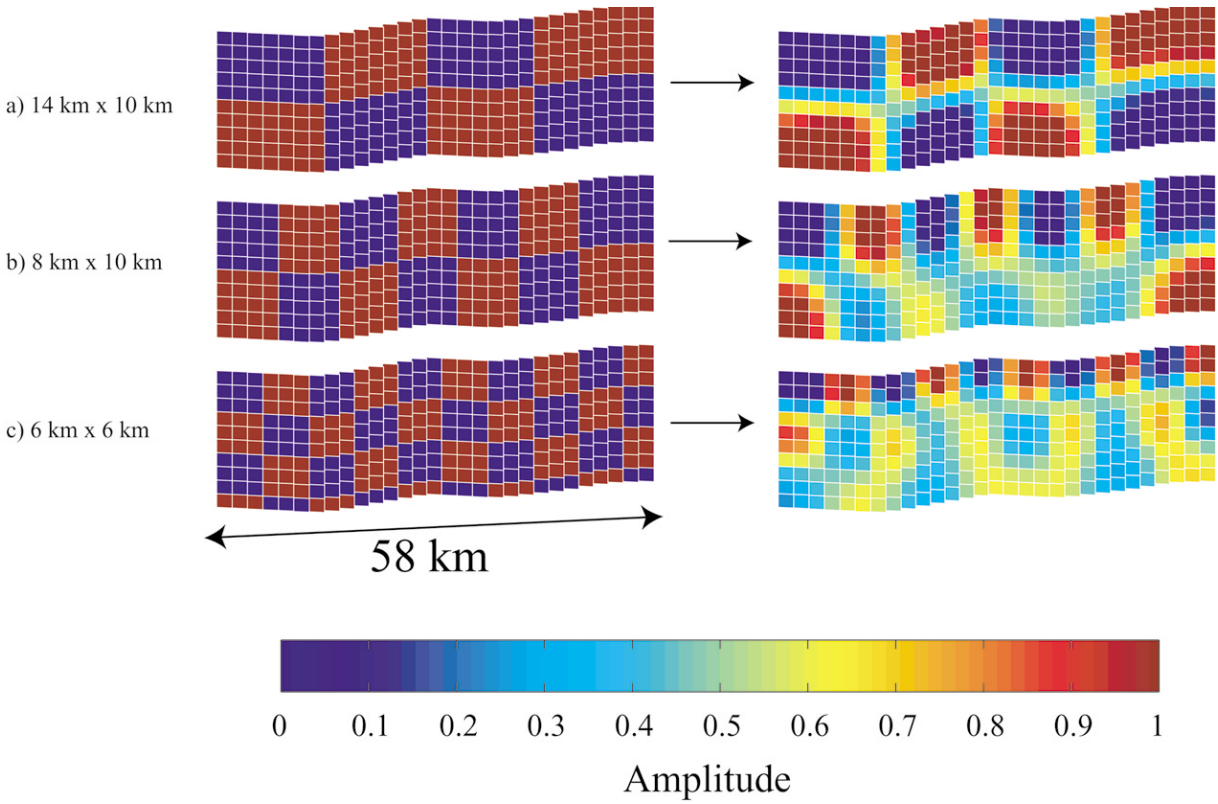

Figure 7. The resolution of the Hector Mine distributed slip model: (a) 14 km by 10 km checks, (b) 8 km by 10 km checks, (c) 6 km by 6 km checks.

is generally shallower than that inferred using GPS data (Fig. 5b), and it contains more detail. North of the hypocenter, the shape of our slip distribution is similar to the one inferred previously by other workers (Feigl and Peltzer, 1993; Feigl and Massonnet, 1995; Massonnet and Feigl, 1998): a large concentration of slip is inferred within the step-over between the Homestead Valley and Camp Rock faults, and a smaller concentration of slip is inferred just north of the hypocenter. The slip inferred using GPS data is similar to that obtained by Freymueller *et al.* (1994), in that we infer a concentration of slip below and north of the hypocenter and a second concentration of slip on the Homestead Valley, Camp Rock, and Emerson faults.

The distribution of slip inferred in the joint inversion of InSAR and GPS data (Fig. 5c) retains features of both slip distributions and leads us to infer a concentration of slip below and north of the hypocenter. The slip then shallows along the Homestead Valley fault and deepens and becomes more intense below the step-over between the Homestead Valley and Emerson faults (Fig. 1) before shallowing once again at the end of the rupture.

Since we allow for a constant offset and tilt of the interferometric displacement map in our inversions, the interferometric displacements are calibrated by the GPS displacements. The constant offset and tilts of the Landers interferogram for our best-fitting distributed slip model are, respectively, 24.5 mm, -0.5 mm/km in the east direction, and 0.04 mm/km in the north direction. This amounts to a one-fringe ambiguity of constant offset, a one-fringe tilt in the east direction, and one-tenth of a fringe tilt in the north direction.

Hector Mine. The distribution of slip on the Hector Mine rupture inferred from InSAR data alone covers a much greater area of the rupture plane than that inferred from GPS data alone and predicts an earthquake moment release nearly twice that predicted by the GPS data. It also leads us to infer deep slip on the rupture and major concentrations of slip to the north of the hypocenter. The slip distribution determined by the joint inversion of GPS and InSAR displacements is bilateral, with a concentration of slip north of the seismologically inferred hypocenter. The slip is mostly confined to the upper 15 km of the rupture plane, but there is an odd concentration of slip between 12 and 16 km on the northern part of the rupture plane. This could be due to unmodeled faulting geometry, deep slip on an alternate strand of the rupture, or postseismic deformation. The magnitude (7.1) of the earthquake inferred from the joint inversion agrees with seismologic estimates. The constant offset and tilts of the Hector interferogram for our best-fitting distributed slip model are, respectively, 30.6 mm, 0.07 mm/km in the east direction, and -0.47 mm/km in the north direction. This amounts to a one-fringe ambiguity of constant offset, a one-third of a fringe tilt in the east direction, and a two-fringe tilt in the north direction.

It is somewhat surprising that the patch of high slip on the southeastern segment of the Hector Mine rupture, inferred from the GPS and joint inversions, was not resolved by inverting the interferogram alone. We attribute this to the fact that there was likely a significant north–south tilt in the interferogram that affected how the inferred slip would be distributed along the rupture's strike. In the inversion of the interferogram alone, slip is concentrated to the north of the hypocenter; it is more evenly distributed, north and south of the hypocenter, in the joint inversion. This distribution is in agreement with the inference, made using seismic broadband displacement data, that slip on the Hector Mine rupture was bilateral (Dreger and Kaverina, 2000; Kaverina et al., 2002).

Boundary Element Modeling

To understand how the Landers earthquake affected the conditions on the Hector Mine rupture and to compute the average stress drop and the orientation of maximum remote compressive stress consistent with each earthquake, we use a boundary element method (BEM) (Crouch and Starfield, 1983). The two ruptures are parameterized as boundaries composed of the same rectangular elements in an elastic half-space Earth model that were used in our geodetic inversions. Given the fault parameterizations and displacement or stress boundary conditions specified normal and tangential to the patches that make up the faults, a BEM can be used to compute stresses and displacements at user-specified observation points (Crouch and Starfield, 1983). The BEM code that we use, Poly3D (Thomas, 1993), allows observation points to be locations within the half-space continuum or the centers of boundary elements, which allows displacements or stresses to be automatically resolved in a coordinate system aligned with each boundary element. Element interactions are included in the solution.

Stress Changes on the Hector Mine Rupture from the Landers Earthquake

We investigate the stress-related interaction between the Landers and Hector Mine earthquakes by using the fault parameterization specified in our linear inversions of geodetic data to define the boundary elements of the Landers and Hector Mine ruptures. To solve for the distribution of stress on the Hector Mine rupture (Fig. 8), we first specify the boundary conditions to be the values of the slip inferred using geodetic data on each element of the Landers rupture. The observation points are the centers of the elements that make up the Hector Mine rupture.

Coseismic Stress Drops and Remote Stress Orientations

In Poly3D, a remote stress tensor can be specified. Because there is a linear relationship between slip on rupture patches and the elements of the remote stress tensor, we were able to use the BEM code to compute Green's functions for use in a linear inversion of slip distributions for the average coseismic stress change most likely to have caused them.

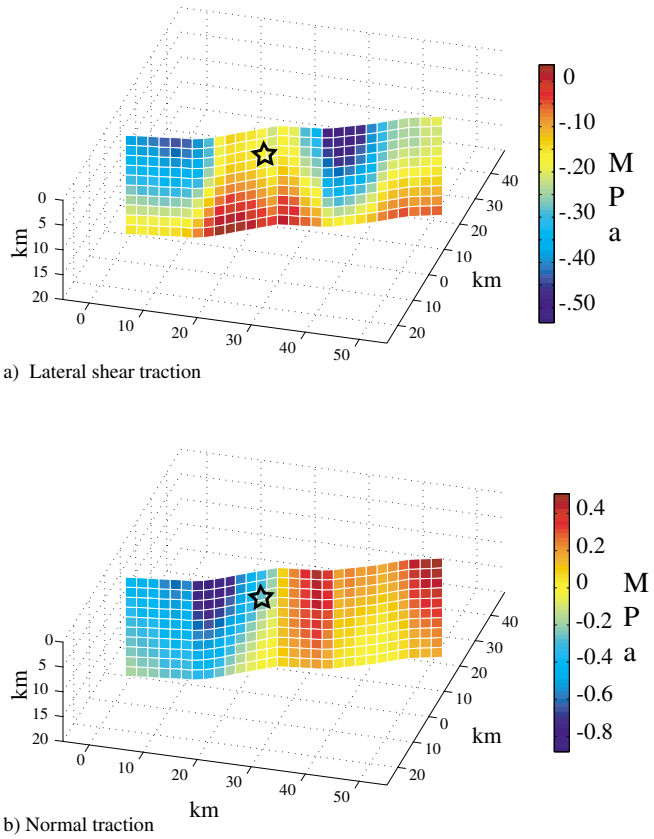

Figure 8. The shear and normal stresses induced by the Landers earthquake resolved onto the Hector Mine rupture planes. Stars mark the position of the Hector Mine hypocenter. (a) Shear traction; (b) normal traction.

From this we can infer a direction of maximum remote compressive stress in the Mojave Desert and the average stress drop on each earthquake rupture.

We use the following system of equations to perform the linear inversion to solve for the components of the stress tensor:

$$\Sigma_m^{-1/2}\,\mathbf{G}\begin{bmatrix}\sigma_{11}\\ \sigma_{22}\\ \sigma_{12}\end{bmatrix} = \Sigma_m^{-1/2}\,\vec{\mathbf{m}}, \qquad (3)$$

where $\vec{\mathbf{m}}$ is a coseismic distributed slip model; $\mathbf{\Sigma}_m$ is the model's covariance matrix; σ_{11}, σ_{22}, and σ_{12} are the components of the two-dimensional stress tensor; and $\mathbf{G}$ contains the Green's functions relating unit changes stress components to slip on the rupture patches.

In these stress inversions, we assume plane stress. This assumption is justified by the microseismic inference that the second principal stress (σ_2) is vertical, on average, in the Mojave Desert (e.g., Hauksson, 1994). We also argue that any average change in σ_2 is small compared to the changes in the other principal stresses. While we do assume plane stress, we use only significant slips on model patches in the inversions for background stress change, so that the overall 3D shape and average slip at various locations on the rupture surface is accounted for. Smaller details of the slip distribution may be due to material heterogeneity or fault geometry complexities that are not accounted for in a simple, homogeneous, elastic half-space Earth model.

BEM Results

Stress Changes on the Hector Mine Rupture from the Landers Earthquake. We use the BEM code to compute the stress changes on the Hector rupture caused by the distribution of slip that we geodetically inferred on the Landers rupture. The results shown in Figure 8 are similar to those obtained by a number of other workers (e.g., Parsons and Dreger, 2000; Scientists of the USGS *et al.*, 2000; Harris and Simpson, 2002). The shear and normal stress changes on the Hector Mine rupture as a result of the Landers earthquake vary spatially. The shear stress is nearly everywhere decreased (Fig. 8a). At the hypocenter, the shear stress is reduced less than at locations at the same depth to the north and south of the hypocenter, and deep below the hypocenter, the shear stress change is nearly zero or positive. After the Landers earthquake, the northern half of the Hector Mine rupture was unclamped (Fig. 8b) but the southern half was clamped.

The Coulomb stress change (ΔCFF), a measure of the balance between the shear stress and the product of the effective coefficient of friction and the normal stress, is often used to evaluate whether a stress-inducing event made it more likely that the crust would break across a specified plane. The Coulomb stress change is

$$\Delta\mathrm{CFF} = \Delta\tau - \mu'\Delta\sigma_n, \qquad (4)$$

where $\Delta\tau$ is the change in shear stress, μ' is the effective friction including the effect of pore-fluid pressure change, and $\Delta\sigma_n$ is the change in normal stress (clamping is positive). ΔCFF increases (planes are more likely to fail) if the shear stress change is positive and/or the normal stress change is negative.

The observation that the predicted spatial distribution of ΔCFF on the Hector Mine rupture resulting from the Landers earthquake (distributions of Landers–Hector Mine ΔCFF are plotted by Parsons and Dreger, 2000; Scientists of the USGS *et al.*, 2000; and Harris and Simpson, 2002) is correlated with most seismologically and geodetically inferred distributions of Hector Mine slip supports the hypothesis that coseismic static stress changes are a major factor in earthquake interactions.

Coseismic Stress Drops and Remote Stress Orientations. The results of the inversion of the slip distributions for the components of the remote stress change are shown in Table 2. We tabulate the azimuth of maximum compressive stress change and the maximum shear stress drop on the earthquake ruptures most likely to have been responsible for the

distributions of slip inferred from geodetic data. The average shear stress drop on the Landers rupture was approximately 8 MPa; the average shear stress drop on the Hector Mine rupture was approximately 10 MPa. The azimuth of maximum compressive remote stress change for both earthquakes is approximately 17°. The estimates of background stress direction and stress drop associated with the Landers earthquake agree favorably with those inferred by others (see the Discussion section).

Rate-and-State Friction

The distribution of the change in the Coulomb failure function (CFF) (Stein and Lisowski, 1983; Oppenheimer *et al.*, 1988) is commonly used to assess whether the probability of rupture on a fault near a recent earthquake has changed. However, the distribution of Coulomb failure stress change induced on the Hector Mine rupture by the Landers earthquake has failed to definitively describe how these two earthquakes were connected (Scientists of the USGS *et al.*, 2000; Harris and Simpson, 2002). One source of confusion could be the assumption in the CFF calculation that the frictional strength of fault surfaces remains constant with time, this may not be the case.

Laboratory experiments have shown that a variety of sliding phenomena can be described using a formula for the frictional resistance that contains not only a static friction term but also depends on the time-varying sliding velocities and states of fault surfaces (Dieterich and Kilgore, 1996; Dieterich, 1979, 1981; Ruina, 1983). Because it has become apparent that the changes in stress normal to the Hector Mine rupture were important in describing the interaction between the Landers and Hector Mine earthquakes (Parsons and Dreger, 2000; Scientists of the USGS *et al.*, 2000), we sought out a model that explicitly accounts for the effects of normal stress changes on time-dependent frictional strengths. In contrast to previous studies that consider only the effects of shear stress changes on time-dependent friction, an algorithm outlined by Linker and Dieterich (1992) explicitly includes the effects of changes in normal stress on changes in the state of the fault surface.

A Computational Spring-and-Slider Model

We use a simple spring-and-slider model (Fig. 9) and a rate-and-state variable friction constitutive law to investigate how the perturbations in stress induced by the Landers earthquake on the Hector Mine rupture may have affected the balance between Hector Mine's frictional resistance and tectonic loading. In contrast to similar and numerous previous studies carried out over the last two decades that considered only shear stress perturbations while holding normal stresses constant (e.g., Dieterich, 1979), we allow perturbations in normal stresses by explicitly including the effect of a change in normal stress on the state of the sliding surface (Linker and Dieterich, 1992).

In a spring-and-slider model, the shear stress at the sliding interface exerted by loading depends on the stiffness of the system and the extension of the spring:

$$\tau_t = \frac{K}{l}(d_t - \delta), \tag{5}$$

where τ_t is the shear stress at the base of the block caused by the pull of the spring, K is the spring stiffness, l is the length of the sliding zone, d_t is the displacement of the loading point, and δ is the displacement of the slider.

The frictional resistance at the base of the block is the product of the normal stress and the rate-and-state dependent friction:

$$\tau_f = \mu\sigma + A\sigma\ln\left(\frac{V}{V^*}\right) + B\sigma\ln\left(\frac{\theta}{\theta^*}\right), \tag{6}$$

where μ is the static friction, A and B respectively control the amplitudes of velocity and state changes on frictional resistance, σ is the normal stress at the sliding interface, V is the velocity of the block, θ is the state of the sliding interface and is proportional to the age of the asperity contacts at the interface, and V^* and θ^* are reference velocity and state (which we set to 1.0).

To investigate the time-dependent frictional behavior

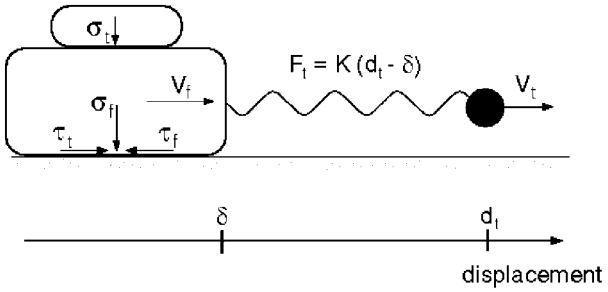

Figure 9. The spring-and-slider system used to conceptualize the interaction between the Landers and Hector Mine earthquakes. τ_t is the shear stress at the base of the block caused by the pull of the spring, τ_f is the frictional resistance to sliding at the interface, K is the spring stiffness, σ_t represents a tectonic normal stress, σ_f represents the lithostatic normal stress, V_f is the velocity of the slider, V_t is the velocity of the load point, d_t is the displacement of the loading point, and δ is the displacement of the slider.

Table 2
The Coseismic Shear Stress Drops Inferred from the Slip Distributions

Rupture	Azimuth of Maximum Compressive stress drop (°)	Shear stress drop (MPa)
Hector Mine	17 ± 6	10 ± 2
Landers	17 ± 4	8 ± 1

that may have occurred on the Hector Mine rupture, we compute the displacement of the slider and the shear stress acting on the sliding interface that corresponds to probable tectonic loading conditions before and after the Landers earthquake. We use a variable time-stepping procedure in which the displacement of the load point, a proxy for tectonic loading, increases proportional to its specified velocity. We assume that, at the center of each time step, the frictional resistance, τ_f, is equal to the shear loading, τ_t. This is accomplished by using a predictor–corrector method to find the velocity of the slider at which the shear stresses are equal (e.g., Linker and Dieterich, 1992). The velocity of the slider is assumed constant throughout the time-step and is used to evolve the state through the time-step. A change in the force (e.g., Landers coseismic stress change) that shears parallel to the sliding interface can be exerted on the system by changing the velocity of the load point and the normal force at the interface can be changed by varying the weight of the block.

The explicit dependence of the state on changes in normal stress proposed by Linker and Dieterich (1992) is included by

$$d\theta = \left(\frac{d\theta}{d\delta}\right)_{\sigma=\text{const.}} d\delta - \frac{\alpha\theta}{B\sigma}\, d\sigma \qquad (7)$$

where $d\theta$ is the change in state, $d\delta$ is a displacement the size of which depends on the velocity of the slider, α is an empirically determined constant that controls the influence of changes in normal stress (see Linker and Dieterich, 1992), and $d\sigma$ is a change in normal stress. The term on the left of the minus sign describes how changes in state depend on the velocity of the slider under constant normal stress; the term to the right of the minus sign describes the dependence of state on changes in normal stress.

Because the state is proportional to the age of the contacts at the sliding surface, the value of the state variable depends on the velocity of the block and the distribution of contacting asperities at the sliding surface. The steady-state value of the state variable is $\theta^{ss} = D_c/V$, where D_c is the characteristic slip distance (Linker and Dieterich, 1992). The nature of D_c has been investigated by a number of workers (see Marone, 1998); it can essentially be considered a measure of the maximum spacing between contacts on the fault surface. Assuming that older faults have smoother surfaces, this rate-and-state friction parameter takes into account the history of slip on a fault.

Implementation

In our computer experiments we start the system and let it settle, so that the velocity of the slider equals the velocity of the load point. We estimate that the velocity of the load point, a proxy for tectonic loading, is 0.08 to 0.8 mm per year (Table 3) using the 10,000- to 50,000-yr range of recurrence interval (e.g., Lindvall et al., 2001) of earthquakes that slip 4 to 8 m (the range of right-lateral slip inferred in our inversions) on the faults that broke during the Hector Mine rupture. We imply that the faults involved in the Hector Mine rupture slid steadily at the depth of the Hector Mine hypocenter before the Landers and Hector Mine earthquakes, because we assume that the block slides steadily before the stress is perturbed.

Using the (1) rate-and-state formulation, (2) a range of values for the rate-and-state friction parameters, (3) normal stresses the size of lithostatic overburden stresses at the range of Hector Mine hypocentral depths (2–8 km) (Scientists of the USGS *et al.*, 2000), and (4) tectonic load point velocities (Table 3), we compute how the frictional resistance (Equation 6) and velocity in the spring-and-slider model evolve with displacement of the slider in response to shear and normal stress perturbations. We convert displacement to time using the velocity of the slider in each time step and plot the time evolution of the frictional resistance relative to its steady-state value after Landers-like stress perturbations (Fig. 10a). We also compute how the frictional resistance (friction stress) evolves with the velocity of the slider relative to its steady-state value at each velocity (Fig. 10b) (e.g., Rice and Gu, 1983).

We choose three pairs of Landers-induced shear and normal stress perturbations predicted at three points on the Hector Mine rupture using the BEM. At the hypocenter, calculations using our slip models predict a normal stress step of -0.3 MPa and a shear stress step of -0.18 MPa. At 16 km north of the hypocenter, within the northern lobe of reduced shear stress. (Fig. 8), our predicted normal stress step is -0.5 MPa and the shear stress step is -0.35 MPa. At 14 km south of the hypocenter, within the southern lobe of reduced shear stress (Fig. 8), our predicted normal stress step is 0.1 MPa, and the shear stress step is -0.35 MPa. For values of static friction less than 0.6, the ΔCFF (Equation 4) is less than zero at each of the three locations.

Rate-and-State Friction Results

The evolution of the frictional resistance within the simple spring-and-slider model corresponding to three points on the Hector Mine rupture is shown in Figure 10a. The steady-state level of shear loading at the hypocentral depth (5 ± 3 km) on the Hector Mine rupture before the Landers earthquake is controlled by the normal stress, the loading rate, and the values of the rate and state parameters (Table 3). Within the range of possible hypocentral depths, the steady-state shear stress is approximately 0.698 times the lithostatically imposed normal stress. As a result of the stress perturbations induced by the Landers earthquake, the shear loading at different locations on the rupture tends toward new steady-state values (Fig. 10b). Since the rate-and-state friction parameters remain the same, these new steady-state values depend on the computed static changes in normal stress induced by the Landers earthquake. Because of the clamping south of the hypocenter, the new steady-state value there is greater than the original steady-state value, so shear

Table 3
The Parameters Used in the Rate-and-State Frictional Modeling

Variable	Value	Range tested	Comment
A	0.0055	0.003 to 0.008	Dieterich (1981)
B	0.0089	$-0.006 \leq (A - B) \leq -0.0007$	Dieterich (1981)
D_c	1 mm	0.001 to 10 mm	Tse and Rice (1986); Cao and Aki (1985). 0.01–0.1 mm: laboratory experiments. 1–10 mm: cracklike rupture models
α	0.38	0.2 to 0.56	Linker and Dieterich (1992)
μ	0.7	0.4 to 0.8	Friction is probably high at the Hector hypocenter (Parsons and Dreger, 2000).
K/l	650 MPa/mm	400 to 900 MPa/mm	Shear modulus $G = 30$ GPa; Poisson's ratio $\nu = 0.25$; $l = 100$ to 44 km; $K = G/(1 - \nu)$
σ	130 MPa	78 to 182 MPa	Lithostatic stress at 3–7 km
V_t	0.4 mm/yr	0.08 to 0.8 mm/yr	Assumes 4–8 m of slip every 10,000 to 50,000 years.

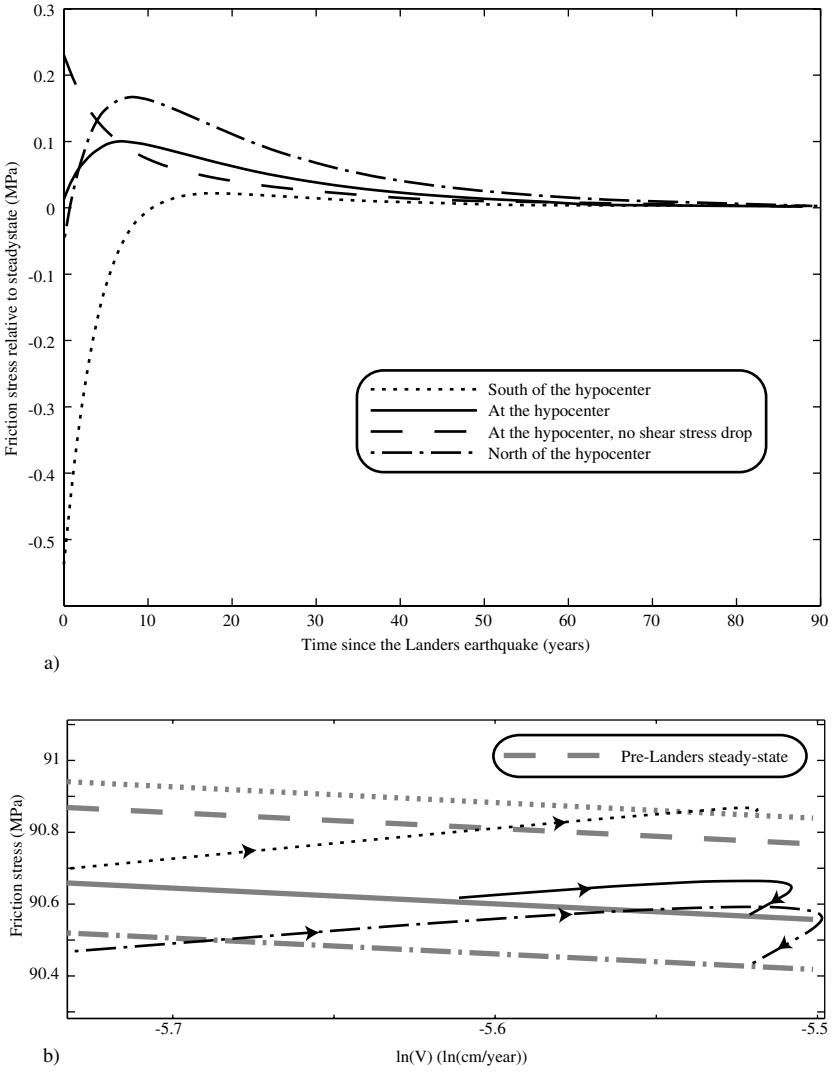

Figure 10. (a) Time-dependent response of the spring-and-slider system with realistic tectonic loading and rate-and-state friction parameters. For all three traces, the normal stress is equal to lithostatic stress at a depth of 5 km (the mean hypocentral depth of the Hector Mine earthquake). Shear loading is plotted relative to steady-state shear loading at the instantaneous velocity of the slider. The evolution of frictional stress is computed for stress perturbations corresponding to points at, 16 km north of, and 14 km south of the Hector Mine hypocenter. The dashed line follows the evolution of friction stress if there had been only a normal stress perturbation similar to what may have occurred at the hypocenter. The shear loading is the frictional resistance (Equation 6) computed using the a constant velocity at the center of each time step determined by equating the frictional resistance (Equation 6) with the shear stress imposed by tectonic loading (Equation 5). (b) The evolution of friction stress as the velocity of the slider changes in response to the stress perturbations. Line styles are for the same cases (stress perturbations at, north, and south of the hypocenter) as indicated in (a). The straight lines are the steady-state values of the friction stress at each velocity. The friction stress evolves to the new steady-state value as the system evolves.

stress must increase to resume steady sliding. Because of the unclamping at and north of the hypocenter, the new steady-state value of shear loading is less than the original steady-state value, and the shear stress must decrease to resume steady sliding. Failure or a strain pulse could be mechanisms for this decrease. For comparison, we indicate in Figure 10 how the frictional resistance at the hypocenter would have evolved if there had been a decrease in normal stress but no change in shear stress.

Examination of the ways that the shear stresses evolve in our simple spring-and-slider model after stress perturbations similar to the ones imposed by the Landers earthquake on the Hector Mine rupture allows us to propose a mechanism for delayed triggering of the Hector Mine earthquake by the Landers earthquake, a mechanism that includes time-dependent friction. At the three locations examined, the shear loading drops sharply right after the Landers earthquake. The amplitude of this drop is equal to the magnitude of the computed static shear stress decrease induced by the Landers earthquake at each location. To the south of the hypocenter, the level to which the shear loading drops is always less than the level at the new steady state, so the amount of crustal movement and seismicity (Wyss and Wiemer, 2000) drops as well. At the hypocenter, the level to which the shear loading drops is slightly greater than the new steady-state level; north of the hypocenter, the initial post-Landers shear loading drop may have reached a sub-steady-state level before rising above that level (Fig. 10a). In both cases, the loading increases with time in response to the reaction of the coupled system to the shear and normal stress changes; however, the shear loading (relative to steady state) north of the hypocenter may have been less than that at the hypocenter for some period of time.

Because the change in the steady-state level of loading is the product of the Landers coseismic normal stress change on the Hector Mine rupture and the steady-state friction, the loading curves (Fig. 10a) can be conceptualized as time-dependent Coulomb stress change indicators. The shear loading would have followed the dashed line in Figure 10a if there had been only a normal stress decrease at the Hector Mine hypocenter right after the Landers earthquake, and the most likely time for a triggered large earthquake would have been immediately after Landers. Because of the shear stress decrease, the most likely time for a large earthquake at this location to be triggered by Landers was postponed by a number of years. At any time, the amount of Coulomb stress change is equal to the difference between the value of shear loading and the value of shear loading at the new steady state. At the Hector Mine hypocenter, the amplitude of the rounded peak is approximately 0.1 MPa (1 bar) above the new steady-state shear loading for nearly the entire range of rate-and-state parameters and loading conditions considered.

We performed a sensitivity test by varying the rate-and-state friction parameters, overburden stress, and load point velocity through the full ranges indicated in Table 3 and noting the effect on peak friction stress and the time delay to that peak after a Landers-like stress perturbation. The result (that the amplitude of the peak in friction stress is 0.1 MPa above the steady-state friction stress) is stable for the entire range of parameters except for the minimum value of α. Holding all other parameters at their middle values, the minimum value of α yields a peak friction stress that is only 0.05 MPa above the steady-state friction stress. The time to peak loading increases with increases in A, D_c, α, and σ(depth) and with decreases in μ, V_{lp}, and K/l. Changes in $A - B$ over the specified range have little effect on the time to peak loading.

We set the parameters to extreme values, corresponding to their tendency to increase or decrease the time to peak loading, to determine a range of possible delays of peak loading after a Landers-like stress perturbation. If all the parameters, including possible load point velocities, are set to values at the edges of the ranges specified in Table 3, the system becomes unstable and the desired behavior is not observed. Thus, we set all parameters to their bounds according to their tendency to increase or decrease the time to peak loading and vary first the load point velocity and then α (if necessary) until curves similar to those shown in Figure 10a are obtained. (An exception is that for values of D_c less than 0.5 mm the desired behavior is not observed, so we set our minimum value of D_c to 0.5 mm.) We compute a time to peak loading of 37 years for $A = 0.008$, $A - B = -0.006$, $D_c = 10$ mm, $\alpha = 0.56$, $K/l = 400$ MPa/mm, $\mu = 0.4$, $V_{lp} = 0.3$ mm/yr, and $\sigma = 182$ MPa. We compute a time to peak loading of 1.2 years for $A = 0.003$, $A - B = -0.0007$, $D_c = 0.5$ mm, $\alpha = 0.23$, $K/l = 900$ MPa/mm, $\mu = 0.8$, $V_{lp} = 0.4$ mm/yr, and $\sigma = 78$ MPa.

Discussion

Geodetic Inversions

Following the Landers earthquake, a number of coseismic slip distributions were inferred using seismic and geodetic data (for a list, see Harris and Simpson, 2002). One feature that most of the slip distributions had in common was that they mapped a high slip concentration extending from the step-over between the Homestead Valley and the Emerson faults onto the Emerson fault (e.g., Wald and Heaton, 1994). Others found high slip concentrations corresponding to possible asperities at several locations along the fault (e.g., Cohee and Beroza, 1994). Our slip model for the Landers earthquake is slightly different from that inferred by workers who jointly inverted seismic and geodetic data (Wald and Heaton, 1994), in that we do not infer a concentration of slip within the step over between the Johnson Valley and the Homestead Valley faults. Their concentration of slip in that location is imposed mostly by their GPS geodetic inversion. Our slip model inferred from the joint inversion of GPS and InSAR data is more similar to their slip model inferred from inversion of strong-motion data.

Our slip model for the Hector Mine earthquake is simi-

lar to those obtained seismically by Kaverina *et al.* (2000) and through joint inversion of seismic and geodetic data by Kaverina *et al.* (2002). The GPS data constrain the long-wavelength surface deformation and the INSAR data allow us to resolve details in the slip distribution. Both geodetic and seismic slip distributions are bilateral and confined to the upper 15 km of the crust. The similarity of the slip distributions implies that most of the earthquake slip was localized and transformed into ground motion measurable by seismometers.

The differences between the estimated slip distributions of both the Landers and Hector Mine earthquakes inferred using InSAR and GPS separately could be due to several factors. Shallow differences could be effected by vertical displacements being mapped into horizontal ones in the InSAR inversion (Price, 1999a) and by the differences in spatial sampling of the geodetic data sets. Deep differences may be the result of interseismic or postseismic slip downdip of the rupture plane, and the different time intervals spanned by the respective data sets. They may also reflect a tilt in the InSAR displacement map caused by errors in the estimation of SAR satellite orbital positions or by long wavelength changes in atmospheric or ionospheric refractivity.

In the Hector Mine inversion the majority of the GPS displacements are west of the rupture, and the concentration of slip south of the hypocenter is in a region poorly resolved by the GPS data. The available continuous GPS measurements were made in the far-field, and the campaign-mode measurements were made anywhere from 2 years before to 2 weeks after the earthquake. In contrast, the InSAR imagery spans 31 days before to 4 days after the earthquake and should include just as much postseismic signal as the campaign GPS data, if not less. We thus attribute the inferred deep slip in the individual InSAR inversion to orbital error.

Although fault discontinuities and step-overs were observed in the field along the Landers and Hector Mine ruptures, we do not include this detail in our models. Since real rocks tend to react to high stress concentrations by fracturing, we believe that the stress concentrations that occur at the ends of cuts in simple, homogeneous elastic-half spaces are unrealistic and adversely affect estimates of slip distributions more than what would be gained by including detailed, surface-observed rupture geometries. Furthermore, since we do not have geodetic displacements immediately adjacent to the ruptures (the GPS sites are not located there and the interferograms become incoherent near the ruptures), we cannot resolve the details of slip on overlapping segments.

A further assumption inherent in elastic half-space Earth models is that the Earth is not rheologically layered. In fact, the Earth is layered, so its elastic moduli change with depth. The effects of using layered Earth models in inversions of geodetic data are currently being investigated by other workers, and it has been found that surface displacements predicted by elastic half-space models agree with those predicted by more realistic, layered models in the near to intermediate field but not in the far-field (e.g., Hearn *et al.*, 2002). This is in qualitative agreement with previous studies examining the differences between surface displacement fields predicted by homogeneous and layered elastic models (e.g., Rybicki, 1971; Savage, 1987). For example, in their model predictions of GPS coseismic displacements of the 1999 M_w 7.5 Izmit, Turkey, earthquake, Hearn *et al.* (2002) find that a layered half-space model requires slip (in the same direction as that of the earthquake) to be added on fault patches below 9 km depth in order to fit the data as well as a homogeneous half-space model would fit. They also find that the differences between far-field displacements predicted by the homogeneous and layered half-space models can be as large as 3 cm. This is larger than the errors in the data. Our current wealth of precise geodetic data is slightly advanced relative to the availability of tested and easy to use elastic Earth models.

BEM Modeling

The magnitude of the stress drop on the Landers rupture is similar to the 8.5 MPa computed independently by Stein *et al.* (1992). The direction (17°) of the maximum remote compressive stress most consistent with the slip distributions of both ruptures agrees with the direction of background stress inferred from the focal mechanisms of microseismic events in the Mojave Desert before the Landers earthquake (~14°) (Hauksson, 1994). Although the moment of the Hector Mine earthquake was less than the moment of the Landers earthquake, the shear stress drop may have been the same or greater, because the rupture area was smaller. Because the geodetic strain rate (Sauber *et al.*, 1986, 1994; Savage *et al.*, 1990) is one-third less at the location of the Hector Mine rupture than at the location of the Landers rupture, it takes a longer period of time to build up the stress necessary for a magnitude 7 earthquake. Hence, an inference of similar levels of fault maturity at the Hector Mine and Landers hypocentral locations is consistent with the combination of geodetic strain rate estimates and paleoseismologic estimates of recurrence intervals.

Stress Triggering Using Rate-and-State Friction

Rate-and-state friction has been invoked to describe the interaction between the 1906 San Francisco earthquake on the San Andreas fault and a 1911 earthquake on the nearby Calaveras fault (Harris and Simpson, 1998). The juxtaposition, dips of the faults, and rakes of slip of the Hector Mine and Landers ruptures are similar to those of the 1906 and 1911 ruptures. However, although the Hector Mine rupture was in the stress shadow of the Landers earthquake, just as the 1911 rupture was in the stress shadow of the 1906 earthquake (Harris and Simpson, 1998), the stress shadow cast by the Landers earthquake on the Hector Mine rupture was not as large as that cast by the 1906 earthquake on the 1911 rupture. In contrast to the conclusion of Harris and Simpson that it is possible that the 1906 earthquake delayed the 1911 earthquake if the faults at the 1911 earthquake hypocenter were already at failure, we conclude that the Landers earthquake could have triggered the Hector Mine earthquake but

that the peak in shear loading was delayed by a period of years.

Our modeling indicates that the rate-and-state Coulomb stress change at the Hector Mine hypocenter may have reached 0.1 MPa (1 bar) within the 7 years following the Landers earthquake. This amount is of the correct order of magnitude for static Coulomb stress changes that can trigger large earthquakes in this region. For example, the Coulomb stress change induced by the Landers earthquake at the Big Bear hypocenter was 0.3 MPa (Harris and Simpson, 1992; Jaume and Sykes, 1992; Stein *et al.*, 1992). In studies that investigate viscoelastic crustal loading of the Hector Mine faults postseismic to the Landers earthquake it is found that the Coulomb stress change from this mechanism at the Hector Mine hypocenter may have been 0.7 to 2 bars (i.e., 0.07 to 0.2 MPa) (Pollitz, 2000; Wang and Jackson, 2000; Freed and Lin, 2001). The sum of the viscoelastic Coulomb stress change and the rate-and-state friction Coulomb stress change may have ultimately been enough to trigger the Hector Mine earthquake.

We may go a step further and ask why the Hector Mine hypocenter nucleated where it did. While there was a cluster of Landers aftershocks near the future location of the Hector Mine hypocenter, there was also a cluster of Landers aftershocks north of its rupture (the Barstow cluster). Why didn't a large event happen near the Barstow cluster? To answer these questions, we should consider not only changes in the CFF but also changes in normal stress on optimally oriented planes brought about by the Landers earthquake and recall that it is the normal stress change that sets the new, post-event, level of steady-state shear loading. Northwest and southeast of the Landers rupture, lobes of clamping normal stress changes occurred on vertical planes trending N30°W, northeast and southwest of the Landers rupture, lobes of unclamping normal stress changes occurred on similarly oriented planes (Scientists of the USGS *et al.*, 2000). Northwest and southeast of the Landers rupture, the change in the Coulomb failure stress on optimally oriented planes was negative (e.g., King *et al.*, 1994) and this finding, when combined with the computed normal stress changes in these regions, makes it doubly unlikely that earthquakes triggered by the Landers event would occur in them.

The M_L 6.5 Big Bear event occurred 3 hours after the Landers earthquake to the southeast of the Landers rupture in a region where there was both unclamping and Coulomb stress increase on optimally oriented planes. The Barstow cluster occurred to the northwest of the Landers earthquake in a region where the Coulomb stress was increased but there was little change in normal stress. Noting that the Barstow cluster did not occur on a previously mapped or obvious fault it is possible that a large earthquake did not nucleate near the Barstow cluster because of previous recent earthquakes on nearby faults (including the 1947 M_L 6.2 dextral Manix earthquake) (Doser, 1990) that affected the stress field there, or the existence of velocity-strengthening materials along the buried fault surface. Some surface deformation over this cluster is apparent in the Landers interferogram (Price and Sandwell, 1998), so it is possible that significant strain occurred at depth. The only other candidate region for an earthquake triggered by Landers is that near the Hector Mine hypocenter. In this region, there was unclamping and decreases in the Coulomb stress surmountable by post-Landers rate-and-state frictional and viscoelastic relaxation mechanisms.

Conclusions

Joint inversions of GPS and InSAR data for slip on earthquake ruptures yield slip distributions of unprecedented detail. Using both types of geodetic data, we can resolve features with 6-km half-wavelengths throughout the upper 10 to 15 km of the crust (Fig. 7). These detailed slip distributions were combined with boundary element methods and frictional modeling to investigate the interactions between the 1992 Landers and 1999 Hector Mine earthquakes. Using boundary element methods, we compute the distribution of static stress on the Hector Mine rupture that was induced by slip on the Landers rupture and find the stress drop associated with each earthquake (7–9 MPa and 8–12 MPa for the Landers earthquake and the Hector Mine earthquake, respectively) and the orientation of remote stress (17° for both events) most consistent with the earthquake slip distributions. Finally, we use the computed static stress drops and published estimates of regional strain in models employing rate-and-state friction to investigate the evolution of loading on the Hector Mine rupture during the years after the Landers earthquake. Using reasonable parameters, we find that the time-dependent Coulomb stress may have been raised by 0.1 MPa by the time of the 1999 Hector Mine earthquake and thus contributed to the delayed triggering of that event.

Acknowledgments

This paper benefited from careful and constructive reviews by Ruth Harris, Brad Hager, and Victoria Langenheim. This research was supported by the Southern California Earthquake Center. SCEC is funded by NSF Cooperative Agreement EAR-8920136 and USGS Cooperative Agreements 14-08-0001-A0899 and 1434-HQ-97AG01718. The SCEC Contribution Number for this article is 571.

References

Agnew, D. C., S. Owen, Z.-K. Shen, G. Anderson, J. Svarc, H. Johnson, K. E. Austin, and R. Reilinger (2002). Coseismic displacements from the Hector Mine, California, earthquake: results from survey-mode GPS measurements, *Bull. Seism. Soc. Am.* **94,** 1355–1364 (this issue).

Arrowsmith, J. R., and D. D. Rhodes (1994). Original forms and initial modifications of the Galway Lake road scarp formed along the Emerson fault during the 28 June 1992 Landers, California, earthquake, *Bull. Seism. Soc. Am.* **84,** 511–528.

Aydin, A., and Y. Du (1995). Surface rupture at a fault bend: the 28 June 1992 Landers, California, Earthquake, *Bull. Seism. Soc. Am.* **85,** 111–128.

Bock, Y., S. Wdowinski, P. Fang, J. Zhang, S. Williams, H. Johnson, J. Behr, J. Genrich, J. Dean, M. van Danselaar, D. Agnew, F. Wyatt, K. Stark, B. Oral, K. Hudnut, R. King, T. Herring, S. Dinardo, W. Young, D. Jackson, W. Gurtner (1997). Southern California permanent GPS geodetic array: continuous measurements of regional crustal defor-

mation between the 1992 Landers and 1994 Northridge earthquakes, *J. Geophys. Res.* **102,** no. B8, 18,013–18,033.

Cao, T., and K. Aki (1985). Seismicity simulation with a mass-spring model and a displacement hardening–softening friction law, *Pure Appl. Geophys.* **122,** 10–24.

Cohee, B. P., and G. C. Beroza (1994). Slip distribution of the 1992 Landers earthquake and its implications for earthquake source mechanics, *Bull. Seism. Soc. Am.* **84,** 692–712.

Crouch, S. L., and A. M. Starfield (1983). *Boundary Element Methods in Solid Mechanics*, Allen and Unwin, Inc., Winchester, Massachusetts, 322 pp.

Dieterich, J. H. (1979). Modeling of rock friction, 1, experimental results and constitutive equations, *J. Geophys. Res.* **84,** 2161–2168.

Dieterich, J. H. (1981). Constitutive properties of faults with simulated gouge, in *Mechanical Behavior of Crystal Rocks*, American Geophysical Monograph 24, N. L. Carter, M. Friedman, J. M. Logan, and D. W. Stearns (Editors), 103–120.

Dieterich, J. H., and B. Kilgore (1996). Implications of fault constitutive properties for earthquake prediction, *Proc. Natl. Acad. Sci.* **93,** 3787–3794.

Doser, D. I. (1990). A re-examination of the 1947 Manix, California, earthquake sequence and comparison to other sequences within the Mojave block, *Bull. Seism. Soc. Am.* **80,** 267–277.

Dreger, D., and A. Kaverina (2000). Seismic remote sensing for the earthquake source process and near-source strong shaking: a case study of the October 16, 1999 Hector Mine earthquake, *Geophys. Res. Lett.* **27,** 1941–1944.

Du, Y., A. Aydin, and P. Segall (1992). Comparison of various inversion techniques as applied to the determination of a geophysical deformation model for the 1983 Borah Peak earthquake, *Bull. Seism. Soc. Am.* **82,** 1840–1866.

Emardson, R., F. Crampe, G. F. Peltzer, and F. H. Webb (1999). Neutral atmospheric delay measured by GPS and SAR, *EOS* **80,** S79.

Feigl, K. L. and G. Peltzer (1993). Estimation of the slip distribution in the June 28 Landers earthquake sequence by inversion of a coseismic radar interferogram, *Eos Trans. AGU Fall Meet. Suppl.* **74,** 183.

Feigl, K. L., and D. Massonnet (1995). Seismology from space: estimation of fault parameters by inversion of radar interferograms, *Eos Trans. AGU Fall Meet. Suppl.* **76,** S196.

Fleming, R. W., and A. M. Johnson (1997). Growth of a tectonic ridge during the Landers earthquake, *Geology* **25,** 323–326.

Freed, A. M., and J. Lin (2001). Delayed triggering of the 1999 Hector Mine earthquake by viscoelastic stress transfer, *Nature* **411,** 180–183.

Freymueller, J., N. E. King, and P. Segall (1994). The co-seismic slip distribution of the Landers earthquake, *Bull. Seism. Soc. Am.* **84,** 646–659.

Gross, S., and C. Kisslinger (1997). Estimating tectonic stress rate and state with Landers aftershocks, *J. Geophys. Res.* **102,** 7603–7612.

Hanssen, R. (1998). Atmospheric heterogeneities in ERS tandem SAR interferometry, DEOS Rept. 98.1.

Harris, R. A., and P. Segall (1987). Detection of a locked zone at depth on the Parkfield, California, segment of the San Andreas Fault, *J. Geophys. Res.* **92,** 7945–7962.

Harris, R. A., and R. W. Simpson (1992). Changes in static stress on Southern California faults after the 1992 Landers earthquake, *Nature* **360,** 251–254.

Harris, R. A., and R. W. Simpson (1998). Suppression of large earthquakes by stress shadows: a comparison of Coulomb and rate-and-state failure, *J. Geophys. Res.* **103,** 24,439–24,451.

Harris, R. A., and R. W. Simpson (2002). The 1999 M_w 7.1 Hector Mine, California, earthquake: A test of the stress shadow hypothesis?, *Bull. Seism. Soc. Am.* **92,** 1497–1512 (this issue).

Hart, E. W., W. A. Bryant, and J. A. Treiman (1993). Surface faulting associated with the June 1992 Landers earthquake, California, *Calif. Geol.* **46,** 10–16.

Hauksson, E. (1994). State of stress from focal mechanisms before and after the 1992 Landers earthquake sequence, *Bull. Seism. Soc. Am.* **84,** 917–934.

Hauksson, E., Jones, L. M., Hutton, K., and D. Eberhart-Phillips (1993). The 1992 Landers earthquake sequence: seismological observations, *J. Geophys. Res.* **98,** 19,835–19,858.

Hearn, E. H., and E. D. Humphreys (1998). Kinematics of the southern Walker Lane belt and motion of the Sierra Nevada block, California, *J. Geophys. Res.* **103,** 27,033–27,049.

Hearn, E. H., R. Bürgmann, and R. E. Reilinger (2002). Dynamics of Izmit earthquake postseismic deformation and loading of the Düzce earthquake hypocenter, *Bull. Seism. Soc. Am.* **92,** no. 1, 172–193.

Hudnut, K. W., and 16 others (1994). Co-seismic displacements of the 1992 Landers earthquake sequence, *Bull. Seism. Soc. Am.* **84,** 625–645.

Irvine, P. J., and R. L. Hill (1993). Surface rupture along a portion of the Emerson fault, *Calif. Geol.* **46,** 23–26.

Jaume, S. C., and L. R. Sykes (1992). Changes in the state of stress on the southern San Andreas Fault resulting from the California earthquake sequence of April to June 1992, *Science* **258,** 1325–1328.

Johnson, A. M., R. W. Fleming, and K. M. Cruikshank (1994). Shear zones formed along long, straight traces of fault zones during the 28 June 1992 Landers, California, earthquake, *Bull. Seism. Soc. Am.* **84,** 499–510.

Kaverina, A., D. Dreger, and E. Price (2002). The combined inversion of seismic and geodetic data for the source process of the 16, October 1999 M_w 7.1 Hector Mine California, earthquake, *Bull. Seism. Soc. Am.* **92,** 1266–1280 (this issue).

King, G. C. P., R. S. Stein, and J. Lin (1994). Static stress changes and the triggering of earthquakes, *Bull. Seism. Soc. Am.* **84,** 935–953.

Lee, J. S., K. W. Hoppel, S. A. Mango, and A. R. Miller (1992). Intensity and phase statistics of multilook polarimetric and interferometric SAR imagery, *IEEE Trans. Geosci. Remote Sens.* **32,** 1017–1028.

Lindvall, S., and 11 others (2001). Paleoseismic investigations of the 1999 *M* 7.1 Hector Mine earthquake surface rupture and adjacent Bullion fault, Twentynine Palms Marine Corps Base, California, *GSA Cordilleran Section and the AAPG Pacific Section Meeting, Abstracts with Programs*, **33,** A-79.

Linker, M. F., and J. H. Dieterich (1992). Effects of variable normal stress on rock friction: observations and constitutive equations, *J. Geophys. Res.* **97,** 4923–4940.

Marone, C. (1998). Laboratory-derived friction laws and their application to seismic faulting, *Annu. Rev. Earth Planet. Sci.* **26,** 643.

Massonnet, D., and K. L. Feigl (1998). Radar interferometry and its application to changes in the Earth's surface, *Rev. Geophys.* **36,** 441–500.

Massonnet, D., M. Rossi, C. Carmona, F. Adragna, G. Peltzer, K. Feigl, and T. Rabaute (1993). The displacement field of the Landers earthquake mapped by radar interferometry, *Nature* **364,** 138–142.

McGill, S. F., and C. M. Rubin (1999). Surficial slip distribution on the central Emerson fault during the June 28, 1992, Landers earthquake, California, *J. Geophys. Res.* **104** (B3), 4811–4834.

Okada, Y. (1985). Surface deformation due to shear and tensile faults in a half-space, *Bull. Seism. Soc. Am.* **75,** 1135–1154.

Oppenheimer, D. H., P. A. Reasenberg, and R. W. Simpson (1988). Fault plane solutions for the 1984 Morgan Hill, California, earthquake sequence: evidence for the state of stress on the Calaveras fault, *J. Geophys. Res.* **93,** 9007–9026.

Parsons, T., and D. S. Dreger (2000). Static-stress impact of the 1992 Landers earthquake sequence on nucleation and slip at the site of the 1999 $M = 7.1$ Hector Mine earthquake, southern California, *Geophys. Res. Lett.* **27,** 1949–1952.

Peltzer, G., F. Crampe, and P. Rosen (1999). The M_w 7.1, Hector Mine, California earthquake: surface rupture, surface displacement field, and fault slip solution from ERS SAR data, *Eos Trans. AGU Fall Meet. Suppl.* **80,** 256.

Peltzer, G., K. W. Hudnut, and K. L. Feigl (1994). Analysis of coseismic surface displacement gradients using radar interferometry: new insights into the Landers earthquake, *J. Geophys. Res.* **99,** 21,971–21,981.

Peltzer, G., P. Rosen, F. Rogez, and K. Hudnut (1996). Postseismic rebound in fault step-overs caused by pore fluid flow, *Science* **273,** 1202–1204.

Pollitz, F., G. Peltzer, and R. Bürgmann (2000). Mobility of continental mantle: evidence from postseismic geodetic observations following the 1992 Landers earthquake, *J. Geophys. Res.* **105,** 8035–8054.

Pollitz, F. F., and I. S. Sacks (2001). Stress triggering of the 1999 Hector Mine earthquake by transient deformation following the 1992 Landers earthquake, *Bull. Seism. Soc. Am.* **92,** 1487–1496 (this issue).

Price, E. J. (1999a). Vertical displacements on the 1992 Landers, California, earthquake rupture from space geodesy and finite-fault elastic half-space modeling, *EOS Trans. AGU Fall Meet. Suppl.* **80,** 142.

Price, E. J. (1999b). Coseismic and postseismic deformations associated with the 1992 Landers, California, earthquake measured by synthetic aperture radar interferometry, *Ph.D. Thesis*, University of California, San Diego.

Price, E. J., and D. T. Sandwell (1998). Small-scale deformations associated with the 1992 Landers, California, earthquake mapped by synthetic aperture radar interferometry phase gradients, *J. Geophys. Res.* **103,** 27,001–27,016.

Rice, J. R., and J. C. Gu (1983). Earthquake aftereffects and triggered seismic phenomena, *Pageoph* **121,** 187–219.

Rockwell, T. K., S. Lindvall, M. Herzberg, D. Murbach, T. Dawson, and G. Berger (2000). Paleoseismology of the Johnson Valley, Kickapoo, and Homestead Valley faults: clustering of earthquakes in the Eastern California Shear Zone, *Bull. Seism. Soc. Am.* **90,** 1200–1236.

Ruina, A. L. (1983). Slip instability and state variable friction laws, *J. Geophys. Res.* **88,** 10,359–10,370.

Rybicki, K. (1971). The elastic residual field of a very long strike-slip fault in the presence of a discontinuity, *Bull. Seism. Soc. Am.* **61,** 79–92.

Sandwell, D. T., L. Sichoix, D. Agnew, and J. Minster (1999). Near-real-time radar interferometry of the M_w 7.1 Hector Mine earthquake, *Eos Trans. AGU Fall Meet. Suppl.* **80,** 257.

Sauber, J., W. Thatcher, and S. C. Solomon (1986). Geodetic measurement of deformation in the central Mojave Desert, California, *J. Geophys. Res.* **91,** 12,683–12,693.

Sauber, J., W. Thatcher, Solomon, S. C., and M. Lisowski (1994). Geodetic slip rate for the eastern California shear zone and the recurrence time of Mojave Desert earthquakes, *Nature* **367,** 264–266.

Savage, J. C. (1987). Effect of crustal layering upon dislocation modeling, *J. Geophys. Res.* **92,** 10,595–10,600.

Savage, J. C., and J. L. Svarc (1997). Postseismic deformation associated with the 1992 $M_w = 7.3$ Landers earthquake, Southern California, *J. Geophys. Res.* **102,** 7565–7577.

Savage, J. C., M. Lisowski, and W. H. Prescott (1990). An apparent shear zone trending north-northwest across the Mojave Desert into Owens Valley, Eastern California, *Geophys. Res. Lett.* **17,** 2113–2116.

Scientists of the U.S. Geological Survey, Southern California Earthquake Center, and California Division of Mines and Geology (2000). Preliminary report on the 16 October 1999 *M* 7.1 Hector Mine, California, earthquake, *Seism. Res. Lett.* **71,** 11–23.

Shen, Z. K., D. D. Jackson, Y. Feng, M. CLine, M. Kim, P. Fang, and Y. Bock (1994). Postseismic deformation following the Landers earthquake, California, 28 June 1992, *Bull. Seism. Soc. Am.* **84,** 780–791.

Sieh, K., L. Jones, E. Hauksson, K. Hudnut, D. Eberhart-Phillips, T. Heaton, S. Hough, K. Hutton, H. Kanamori, A. Lilje, S. Lindvall, S. F. McGill, J. Mori, C. Rubin, J. A. Spotila, J. Stock, H. K. Thio, J. Treiman, B. Wernicke, and J. Zachariasen (1993). Near-field investigations of the Landers earthquake sequence, April to July 1992, *Science* **260,** 171–176.

Simons, M., Y. Fialko, C. Ji, M. Pritchard, P. Rosen (1999). Analysis of surface deformation from the *M* 7.1 Hector Mine, CA earthquake of 10/16/99, *EOS Trans. AGU Fall Meet. Suppl.* **80,** 258.

Sowers, J. M., J. R. Unruh, W. R. Lettis, and T. D. Rubin (1994). Relationship of the Kickapoo fault to the Johnson Valley and Homestead Valley faults, San Bernardino County, California, *Bull. Seism. Soc. Am.* **84,** 528–536.

Spotila, J. A., and K. Sieh (1995). Geologic investigations of a "slip gap" in the surficial ruptures of the 1992 Landers earthquake, southern California, *J. Geophys. Res.* **100** (B1), 543–559.

Stark, P. B. and R. L. Parker (1995). Bounded variable least squares: an algorithm and applications, *Comput. Stat.* **10,** 129–141.

Stein, R. S., and M. Lisowski (1983). The 1979 Homestead Valley earthquake sequence, California: control of aftershocks and postseismic deformation, *J. Geophys. Res.* **88,** 6477–6490.

Stein, R. S., G. C. P. King, and J. Lian (1992). Change in failure stress on the southern San Andreas fault system caused by the 1992 magnitude = 7.4 Landers earthquake, *Science* **258,** 1328–1332.

Tarayre, J., and D. Massonnet (1996). Atmospheric propagation heterogeneities revealed by ERS-1 interferometry, *Geophys. Res. Lett.* **23,** 989–992.

Thomas, A. L. (1993). Poly3D: A three-dimensional, polygonal element, displacement discontinuity boundary element computer program with applications to fractures, faults, and cavities in the Earth's crust, *Master's Thesis*, Stanford University, Stanford, California.

Tse, S., and J. Rice (1986). Crustal earthquake instability in relation to the depth variation of frictional slip properties, *J. Geophys. Res.* **91,** 9452–9472.

Wald, D. J., and T. H. Heaton (1994). Spatial and temporal distribution of slip for the 1992 Landers, California, earthquake, *Bull. Seism. Soc. Am.* **84,** 668–691.

Wang, H., and D. D. Jackson (2000). Stresses on the Hector Mine fault from tectonics, co-seismic stress, and viscoelastic relaxation, *Eos Trans. AGU Fall Meet. Suppl.* **81,** 149.

Wdowinski, S., Y. Bock, J. Zhang, P. Fang, and J. Genrich (1997). Southern California permanent GPS geodetic array; spatial filtering of daily positions for estimating coseismic and postseismic desplacements induced by the 1992 Landers earthquake, *J. Geophys. Res.* **102,** 18,057–18,070.

Wiemer, S., and M. Wyss (1994). Seismic quiesence before the Landers ($M = 7.5$) and Big Bear ($M = 6.5$) 1992 earthquakes, *Bull. Seism. Soc. Am.* **84,** 900–916.

Williams, S., Y. Bock, and P. Fang (1998). Integrated satellite interferometry: tropospheric noise, GPS estimates and implications for interferometric synthetic aperture radar products, *J. Geophys. Res.* **103,** 27,051–27067.

Wyss, M., and S. Wiemer (2000). Change in the probability for earthquakes in Southern California due to the Landers magnitude 7.3 earthquake, *Science* **290,** 1334–1338.

Zachariasen, J., and K. Sieh (1995). The transfer of slip between two en echelon strike-slip faults: a case study from the 1992 Landers earthquake, southern California, *J. Geophys. Res.* **100** (B8), 15,281–15,301.

Zebker, H. A., P. A. Rosen, R. M. Goldstein, A. Gabriel, and C. L. Werner (1994). On the derivation of coseismic displacement fields using differential radar interferometry: the Landers earthquake, *J. Geophys. Res.* **99,** 19,617–19,743.

Zebker, H. A., P. Segall, F. Amelung, and S. Jonsson (1999). Slip distribution of the Hector Mine earthquake inferred from interferometric radar, *Eos Trans. AGU Fall Meet. Suppl.* **80,** 258.

The Geophysical Institute
University of Alaska–Fairbanks
P.O. Box 757320
Fairbanks, Alaska, 99775-7320
(E.J.P.)

Department of Earth and Planetary Science
Berkeley Seismological Laboratory
307 McCone Hall
University of California–Berkeley
Berkeley, California 94720
(R.B.)

Manuscript received 19 January 2001.